Investigation of Erosion and Deposition of Sand Particles within a Pin Fin Array

Jonathan B. Cowan

Thesis submitted to the faculty of the Virginia
Polytechnic Institute and State University in partial fulfillment for the
degree of

Master of Science
in
Mechanical Engineering

Danesh K. Tafti – Chair
Srinath V. Ekkad
Mark R. Paul

December 3, 2009
Blacksburg, Virginia

Keywords: Computational Fluid Dynamics, Pin Fin, Particle, Erosion, Deposition

Investigation of Erosion and Deposition of Sand Particles within a Pin Fin Array

Jonathan B. Cowan

ABSTRACT

The transport of particulates within both a fully developed and developing pin fin arrays is explored using computational fluid dynamics (CFD) simulations. The simulations are carried out using the LES solver, GenIDLEST, for the fluid (carrier) phase and a Langragian approach for the particle (dispersed) phase. A grid independency study and validation case versus relevant experiments are given to lend confidence to the numerical simulations. Various Stokes numbers (0.78, 3.1 and 19.5) are explored as well as three non-dimensional particle softening temperatures (θ_{ST} = 0, 0.37 and 0.67). The deposition is shown to increase with decreasing particle Stokes number and thus decreasing size from 0.005% for St_p = 19.5 to 13.4% for St_p = 0.78 and is almost completely concentrated on the channel walls (99.6% - 100%). The erosion potential is shown to increase with Stokes number and is highest on the pin faces. As is to be expected, the deposition increases with decreasing softening temperature from 13.4% at θ_{ST} = 0.67 to 79% for θ_{ST} =0. Overall, the channel walls of the array show the greatest potential for deposition. On the other hand, the pin faces show the greatest potential for erosion. Similarly, the higher Stokes number particles have more erosion potential while the lower Stokes number particles have a higher potential for erosion.

Acknowledgements

This thesis has taken many hours of work and dedication on my part. It is the culmination of 17 years of schooling and at the same time just the beginning of my engineering career. However, many others have helped me along my way to completion of this project and deserve credit.

First, I would like to thank my advisor, Dr. Danesh Tafti. He has given me extraordinary guidance through all aspects of the project. He has guided my exploration of computational fluid dynamics and been a tremendous source of knowledge on the subject. He provided funding for my master's work so that I could continue my education without any financial burden. Dr. Tafti was always accommodating and was always available for help. For these reasons, I give him many thanks.

I would also like to thank my committee members, Dr. Srinath Ekkad and Dr. Mark Paul. Both have given their time to be a member of my committee and to review my work. For that I am very thankful.

Next, I would like to thank Dr. Atul Kohli and Pratt and Whitney for sponsoring my master's work. Atul provided guidance on Pratt and Whitney's requirements for the project and what the next step should be. Pratt and Whitney was also the sponsor of the work and for that I am very grateful.

I would also like to thank my HPCFD lab mates: Pradeep Gopalakrishnan, Mohammad Elyyan, Sai Shrinivas, Naresh Selvarasu, Jose Tijiboy, Sunil Patil, Amit Amritkar, Kohei Takamuku, Nagendra Krishnamurthy, Vivik Sethapati, Surya Deb, and Kamal Viswanath. All of you guys have been extremely helpful in both answering my questions and being brainstorming partners. Without all of your help, this project would have taken much longer and involved many more mistakes.

Along with the colleagues I know in my lab, I would like to thank all the researchers, scientists and engineers who have made contributions to their respective fields. Without all your prior achievements, I could not complete this work and I thank you all.

Finally, I would like to thank my friends and family. In particular, I would like to thank my parents, John and Debbie Cowan, for their 23 years of unconditional love and support. Without their support and motivation, I would not be the person I am today. I would like to thank my brother, Joey Harris, for his support and all the brotherly competition throughout my life to push me farther as a person and a scholar. I would like to thank all my friends both at home and here at Virginia Tech. Over my five and a half years of tenure at this great institution, you all have given many good times and been there to help me through the bad. Thanks guys and gals. Last but not least, I would like to thank my girlfriend Brittany Sanders. She has been a steady source of support and encouragement over the last three years and believes in me more than I believe in myself. For that I am ever grateful.

Dedication

To God and all the people trying to understand and improve this crazy and complex world you have created.

Table of Contents

List of Figures

List of Tables

Nomenclature

A = area, m^2

A_{min} = minimum cross-sectional area, m^2

C_D = drag coefficient

c_p = specific heat capacity, J/kgK

D = pin diameter, m

D_H = hydraulic diameter, $D_H = \frac{4 \times \text{Area}}{\text{Perimeter}}$, m

D_p = particle diameter, m

e_x = x-direction unit vector

F = force, N

f = friction factor, see Equation 3-12

g = gravitational constant, 9.81 m/s^2

H = channel height, m

h = heat transfer coefficient, W/m^2K

h_r = radiative heat transfer coefficient, W/m^2K

k = thermal conductivity, W/mK

L = length, m

L_x = length of domain in streamwise direction, m

m = mass

N = number of rows in the streamwise direction

Nu = Nusselt number, $Nu = \frac{hD}{k}$

$\overline{\text{Nu}}$ = array averaged Nusselt number

ΔP = Pressure drop across array, N/m^2

P = pressure, N/m^2

p = periodic pressure fluctuations, N/m^2

Pr = Prandtl Number

Q_x = volume flow rate, m^3/s

q = heat flux, W/m^2

Re = Reynolds number, $\text{Re} = \frac{\rho u D}{\mu}$

Re_p = particle Reynolds number, $\text{Re} = \frac{\rho_f |u_f - u_p| D_p}{\mu}$

S_ρ = ratio of particle to fluid density, $S = \frac{\rho_p}{\rho_f}$

S = spanwise pin spacing, m

St = Stokes number, see Equation 2-12

T = temperature, K

T_o = non-dimensionalization temperature. See Section 2.2

t = time, s

u = velocity in x-direction, m/s

u_{max} = average velocity at A_{min}, m/s

u_τ = friction velocity. See Equation 3-3.

W = diagonal distance between pins, $W = \left(X^2 + \frac{1}{4}S^2\right)^{\frac{1}{2}}$, m

X = streamwise pin spacing, m

x = streamwise direction

x_p = particle direction

y = vertical direction

z = spanwise direction

Greek Symbols:

β = mean pressure gradient, Pa/m

γ = time dependent temperature gradient, K

ϵ = emissivity, $\epsilon = 1$

θ = non-dimensional temperature

μ = viscosity, kg/ms

ν = kinematic viscosity, m^2/s

ρ = density, kg/m^3

σ = Stefan-Boltzman constant, 5.670 x 10^{-8} W/m^2K^4

τ = non-dimensional time constant

τ_{eq} = equivalent shear stress, N/m^2

ϕ = periodic temperature fluctutations, K

Ω_s = heat transfer area, m^2

Subscripts:

bulk = bulk mean quantity

conv = convective heat transfer

f = fluid

i = index

inlet = at domain inlet

max = taken at minimum cross sectional area

p = particle

rad = radiative heat transfer

ref = reference value

ST = softening temperature

t = turbulent

τ = friction velocity based parameter

w = wall

Superscripts/ accents:

* = non-dimensional term

$\rightarrow$ = vector quantity

Chapter 1
Introduction

Gas turbines used in aircraft are operated in a variety of environments ranging from arctic to desert conditions and everywhere in between. Desert areas present a particular challenge to gas turbine operation because of particulate matter that can be ingested into the engine when the engine operates near ground level. Ingested particles upon entering the gas turbine must travel through the engine or be deposited within it. Hamed and Tabakoff give a lengthy review into the effect of particle ingestion in a gas turbine [1]. Hamed and Tabakoff's review however concerns itself mainly with deposition and erosion on compressor and turbine blades. Another area where erosion and deposition may occur is within the cooling channels of the turbine blades themselves. Cool air is bled off the compressor and fed through the cooling channels within the turbine blades in order to cool them. Particles suspended in this bleed air may then erode or deposit depending on conditions within these channels. Erosion can lead to reduced heat transfer due to geometrical changes to the channel. On the other hand, deposition can lead to blockage of the cooling channel in addition to reduced heat transfer caused by fouling layer build up. Both of these processes are very detrimental as the cooling of the blades is what keeps the blade's structural integrity in the hot turbine section.

One method used to increase heat transfer within the turbine blades is by augmenting the surface through the addition of flow disturbances. Common forms of augmentation include pin fin arrays of various shapes and layouts as well as ribs at varying angles to the flow. Of particular interest to the current investigation is the use of short (H/D ~ 1) pin fin arrays. Figure 1-1 shows a common layout for the cooling passages of a turbine blade. The pin fin region of interest is highlighted.

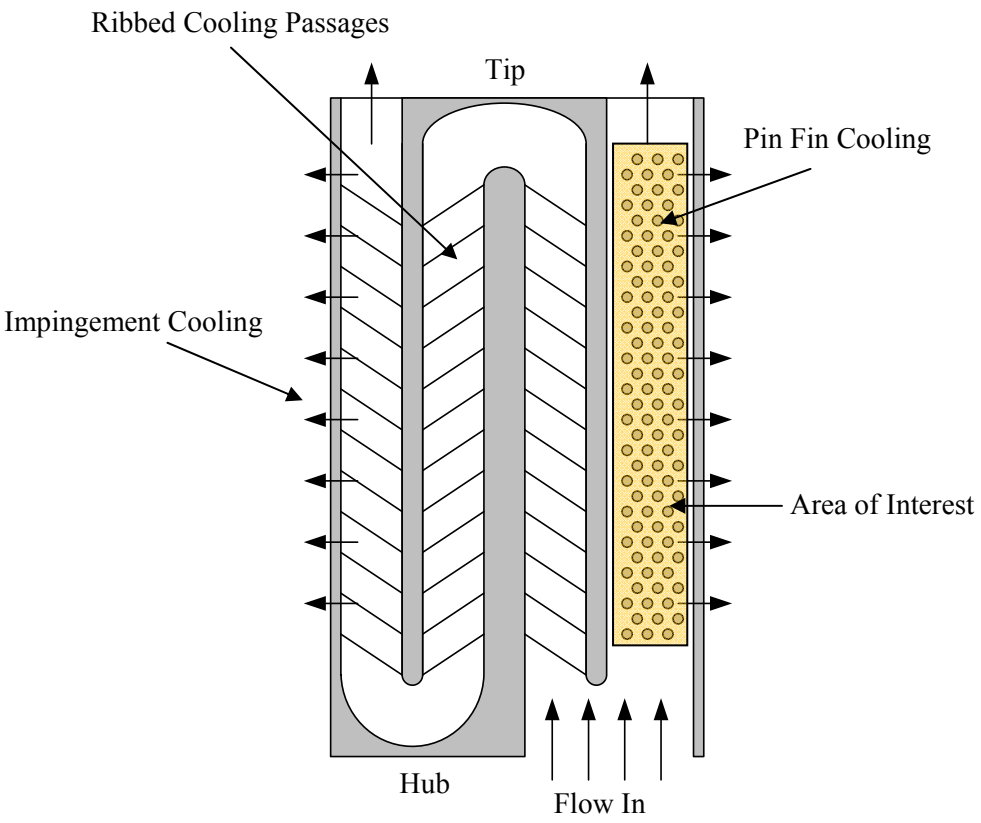

Figure 1-1: Common layout for turbine cooling passages

Extensive experiments on the fluid-thermal characteristics of short pin fin arrays for use in turbine cooling blades have been carried out over the last few decades. Metzger et al. [2] were among the first to perform experiments on the development of Nusselt number in a short pin fin array. These experiments were later extended to additional studies with geometry variations and flow visualization [3, 4]. The results, including Metzger's, of many previous and subsequent pin fin array experiments up to 1989 are reviewed by Armstrong and Winstanley [5]. Chyu et al. further explored short pin fin arrays with and without endwall fillets using naphthalene sublimation [6, 7]. Chyu's finding supported the findings of Metzger. More recently, Ames et. al. [8] have investigated how the heat transfer distribution on the pin surface varies with row number and Reynolds number.

The characteristics of particles within pin fin arrays have been explored by numerous previous researchers. One early technique was the use of analytical methods. Healy [9] used perturbation theory to

describe particles in potential flows. He found a critical Stokes number of 0.125 above which the particle impacts the cylinder. Vittal and Tabakoff [10] explored particles impacting cylinders in both inviscid potential flows and viscous flows. Their research showed two major conclusions. First, the larger particles investigated could travel well upstream due to the collision with the cylinder. This is caused by the increased momentum of the larger particles, which prevents the fluid from quickly changing the particle's trajectory. Secondly, the two different analytical solutions showed that the viscous boundary layer caused the effect of the pin to be felt by the particles well before what the inviscid solution indicates.

Tian et al. [11] numerically investigated particles within an inline pin fin array. For small particles, they found that particles become entrained in the wake regions of the pin and are more subject to turbulent variations. For the largest particles studied, the particles are controlled more by their momentum and the average rebound distance is much longer than for smaller particles. Tian et al. also investigated the effect of surface roughness and showed an increase in particle dispersion with the introduction of surface roughness. Morsi et al. [12] also investigated particles within an inline tube bank. Similar to Tian, they showed that the rebound distance off the pin increases with Stokes number. This led to more dispersion in particle trajectories which in turn led to more uniform erosion of the pins. Morsi also mentioned that the lower Stokes number particles are more likely to erode the 2^{nd} row of tubes. Jun and Tabakoff [13] numerically explored particles within an in-line array of tubes. Though their simulation was for a laminar flow, they showed how particle size affects cylinder impacts. They noted that higher Stokes number particles are more likely to impact the backside of the previous pin row or neighboring pins in the same row.

Fewer studies have been conducted for particles in staggered arrays. Fan et.al [14] simulated the first two rows of a tube bank in a 2-D domain with Stokes numbers ranging from approximately 1 to 25. The smaller particles showed few impacts with the first pin with increased impacts at the second pin. Fan et al. stated that the reason for this increase was the acceleration of the flow past the first row. Jin and Fan

furthered the earlier work of Fan by exploring erosion characteristics of a staggered array [15]. They showed how the impact angle and collision frequency distributions changed with particle size. Of note is how for the 2nd row the collision frequency distribution increases greatly over the first quarter of the pin surface. Also, the point of maximum collision frequency moves further along the pin surface with increasing particle size. Note that all particle studies mentioned above are conducted using a 2-D domain. Thus, effects of end walls on particle motion are not available.

In a similar framework to the pin fin studies, Shah and Tafti [16] explored particle erosion within a ribbed cooling duct. The particles ranged in Stokes numbers, based on friction velocity, from 0.07 to 6.9. They found that the front of the rib was most susceptible to particle impingement. Also, they observed that larger particles bounce off the front of the rib and hit the back of the previous rib due to the particle's increased momentum. Shah and Tafti [17] extended this study to a rotating ribbed duct and found that in a fully-developed flow, the particles tended to accumulate along the side walls of the duct with few particles in the vicinity of the leading and trailing walls of the duct.

The current investigation is into the behavior of particles within a staggered pin fin array. The conditions of the flow within the array are set to mimic those of a turbine cooling blade. Two geometries will be explored, a fully developed pin fin array and a developing pin fin array. Of particular interest is the effect of the sand particle's Stokes number and softening temperature on the deposition and erosion characteristics.

In Chapter 2, the governing equations and mathematical models for solving the multiphase field will be reviewed. Chapter 3 will give validation of the pin fin array using available experimental data. Chapter 4 will investigate the erosion and deposition characteristics of a fully developed pin fin array as well as give a grid independency study and particle force magnitude analysis. Chapter 5 investigates the erosion and

deposition characteristics within a developing flow pin fin array. Finally, Chapter 6 gives a summary and conclusion.

Chapter 2

Governing Equations and Mathematical Models

This section reviews the governing equations and models used in the current simulations. The calculation consists of two phases, the dispersed (particle) and carrier (fluid) phase. The dispersed and carrier phases are solved in the Langragian and Eulerian framework, respectively. In the Langrangian framework, particles are tracked individually with their equations of motion solved at each time step. In the Eulerian framework, the fluid phase is solved using a finite volume method.

2.1 Carrier Phase

The multi-block incompressible LES code GenIDLEST is used to solve the carrier phase [18, 19]. The code solves the incompressible non-dimensional Navier-Stokes and energy equations in a generalized computation space. These equations in physical space as solved by GenIDLEST are given as

$$\vec{\nabla} \cdot \overrightarrow{u^*} = 0 \tag{2-1}$$

$$\frac{\partial \overrightarrow{u^*}}{\partial t^*} + \vec{\nabla} \cdot \left(\overrightarrow{u^*}\,\overrightarrow{u^*}\right) = -\nabla P^* + \vec{\nabla} \cdot \left(\left(\frac{1}{Re} + \frac{1}{Re_t}\right)\vec{\nabla}\,\overrightarrow{u^*}\right) \tag{2-2}$$

$$\frac{\partial \theta}{\partial t^*} + \vec{\nabla} \cdot \left(\overrightarrow{u^*}\theta\right) = \vec{\nabla} \cdot \left(\left(\frac{1}{Re\,Pr} + \frac{1}{Re_t Pr_t}\right)\vec{\nabla}\theta\right) \tag{2-3}$$

where

$$Re = \frac{\rho u_{ref} L_{ref}}{\mu_{ref}},\ Pr = \frac{\mu_{ref}\, c_{p_{ref}}}{k_{ref}},\ Re_t = \frac{\rho u_{ref} L_{ref}}{\mu_t},\ Pr_t = \frac{\mu_t\, c_{p_{ref}}}{k_{ref}}$$

and the following non-dimensionalizations are used

$$u^* = \frac{u}{u_{ref}},\ L^* = \frac{L}{L_{ref}},\ P^* = \frac{P - P_{ref}}{\rho u_{ref}^2},\ t^* = \frac{t L_{ref}}{u_{ref}},\ \theta = \frac{T - T_{ref}}{T_o}.$$

The code solves the above equations in a generalized computation space through a transformation from physical to computational space. To simulate the effect of turbulence, a LES model is used. The dynamic

Smagorinsky model [20, 21] is used to calculate the sub-grid stresses and resolve the turbulent viscosity, μ_t. Discretization is achieved through a second order non-staggered finite volume approach. The solution solver uses a two-step semi-implicit predictor-corrector method for temporal advancement. Further details about the solver can be found in Tafti [18, 19] .

2.2 Dispersed Phase

The dispersed phase is solved using a Langrangian approach in which the particles are individually tracked though out the domain. The particles are assumed perfectly spherical and to exist as point masses. The coupling between the phases is one-way from the carrier to the dispersed phase. Implicit in this is the assumption that the dispersed phase is dilute and does not affect the carrier phase. Portela and Oliemans [22] showed that the effect of particles is to create a damping effect on the turbulence of the fluid by reducing the magnitude of turbulent fluctuations. However, when the volume fraction of particles is small as would be the case in the real application, this effect is minor and one way coupling is a valid assumption.

The basic governing equations for the dispersed phase model are

$$\frac{d\overrightarrow{u_p}}{dt} = \vec{F} \; ; \frac{d\overrightarrow{x_p}}{dt} = \overrightarrow{u_p} \qquad 2\text{-}4$$

which is essentially Newton's 2nd law relating particle acceleration to the instantaneous specific forces (normalized by the particle's mass, m_p) acting on the particle. Kleinstreuer [23] divided the forces into two groups of volume and surface forces. Using this,

$$\frac{d\overrightarrow{u_p}}{dt} = \Sigma\vec{F}_{volume} + \Sigma\vec{F}_{surface} \qquad 2\text{-}5$$

where

$$\Sigma\vec{F}_{volume} = \vec{F}_{gravity} - \vec{F}_{virtual\ mass} = \frac{(m_p - m_f)}{m_p}\vec{g} - \frac{1}{2}\frac{m_f}{m_p}\frac{d_p(\overrightarrow{u_p} - \overrightarrow{u_f})}{dt} \qquad 2\text{-}6$$

and

$$\Sigma\vec{F}_{Surface} = \vec{F}_{drag} + \vec{F}_{pressure} + \vec{F}_{Basset} + \vec{F}_{lift} + \vec{F}_{interaction} \quad 2\text{-}7$$

Starting with Equation 2-6, the first term is the net force acting on the particles due to gravitational forces. This term can be neglected since the mass of the particle is very small and the rotation within a gas turbine would cause gravity's acceleration in one particular direction to be negligible. The second term is the virtual mass force. This force represents the added force needed to accelerate the fluid around the particle as that particle accelerates and can be neglected when the density ratio is very high. Armenio and Fiorotto [24] verify these assumptions.

Looking at Equation 2-7, the drag force of a solid spherical particle is

$$\vec{F}_{Drag} = \frac{1}{2} C_D \rho_f \left(\vec{u_f} - \vec{u_p}\right)\left|\vec{u_f} - \vec{u_p}\right| \frac{\pi {D_p}^2}{4 m_p} \quad 2\text{-}8$$

For particle Reynolds number of less than 800, the drag coefficient as given by Schiller and Nauman [25]

$$C_d = \frac{24}{Re_p}\left(1 + 0.15 Re_p^{0.687}\right) \quad 2\text{-}9$$

is used, where Re_p is the particle Reynolds number and is defined as

$$Re_p = \frac{\rho_p \left|\vec{u_f} - \vec{u_p}\right| d_p}{\mu_f} \quad 2\text{-}10$$

The other terms of the surface forces equation (Equation 2-7) will be shown to be negligible below. The pressure force which accounts for pressure gradients across the particle was shown by Armenio and Fiorotto [24] to be negligible for particles with density ratios greater than the order of one. The Basset force is a history term to account for the temporal changes in the fluid velocity over the integration time. The Basset force to Stokes drag ratio is shown by Kleinstreuer [23] to scale on inverse of the density ratio, thus for the particles considered, i.e. high density ratio, the force is negligible. This result is also found by McLaughlin [26]. Lift forces are caused by high shear gradients in the fluid. This can be

neglected for most particles under most fluid conditions since the shear gradients across the particle are not substantial enough to cause lift. Note, however, that near wall this assumption of negligible lift would fail. McLaughlin [26] showed that the drag force dominates the lift force except in the viscous sub-layer where the lift force is approximately one-third the magnitude of the drag force. Since the viscous sublayer is a small region and since the particle's momentum will cause a lag in the effect of the lift force, this term may be neglected. The final force is the interaction force. This force may comprise many types of interaction forces such as Brownian motion due to molecular interactions, or particle to particle collisions. Note that since all cases of interest in this study involve dilute suspensions, particle-particle interactions are negligible and all particles are well above the molecular scales making Brownian motion negligible. Also in an LES of the continuous phase, the unsteady effect of turbulent eddies is directly captured by the instantaneous representation of the drag force. The effect of subgrid fluctuations is small in a well resolved LES and is neglected.

Since the remaining terms of Equation 2-7 are negligible, the final non-dimensional form of the particle equation of motion is

$$\frac{d\overrightarrow{u_p^*}}{dt^*} = -\frac{1}{St_p}(1 + 0.15{Re_p}^{0.687})(\overrightarrow{u_p^*} - \overrightarrow{u_f^*}) \qquad 2\text{-}11$$

where St_p is the Stokes number which characterizes the ratio of particle time scale to the fluid time scale. St_p is defined as

$$St_p = \frac{\tau_p}{\tau_f}, \qquad \tau_p = \frac{D_p^2\, S_\rho}{18\nu} \quad \text{and} \quad \tau_f = \frac{L_{ref}}{u_{ref}} = \frac{D}{u_{max}} \qquad 2\text{-}12$$

where, S_ρ is the ratio of particle density to fluid density, ν is the kinematic viscosity, L_{ref} is the characteristic length scale (pin diameter D), and u_{ref} is the characteristic velocity (u_{max}). Essentially the Stokes number is a measure of how quickly the particle reacts to changes in the fluid flow around it. A

high Stokes number (>1) means that the particle has more inertia and takes longer to react to any changes in the fluid flow around it. A lower Stokes number (<1) means that the particle responds to changes in the fluid around it quickly and closely follows the flow streamlines.

The deposition model uses the temperature of the particle to determine whether a particle deposits. At each time step, the heat transfer to the particle is determined using

$$\frac{dT_p}{dt} = \frac{6h}{\rho_p c_p D_p}\left(T_f - T_p\right) + \frac{6\epsilon\sigma}{\rho_p c_p D_p}\left(T_w^4 - T_p^4\right) \quad 2\text{-}13$$

In Equation 2-13, the first term on the right hand side represents the convective heat transfer from the carrier phase to the particle and the second is radiation heat transfer from the surroundings to the particle. For a particle assumed to be a sphere, the heat transfer coefficient can be found using the Ranz and Marshall correlation [27] given as

$$\frac{hD_p}{k_f} = Nu = 2.0 + 0.6\sqrt{Re_p}Pr^{1/3}. \quad 2\text{-}14$$

Non-dimensionalizing yields

$$\frac{d\theta_P}{dt^*} = \frac{1}{St_{conv}}\left(\theta_f - \theta_p\right) + \frac{1}{St_{rad}}\left(\theta_w - \theta_p\right) \quad 2\text{-}15$$

where, as before, θ is the non-dimensional temperature given by $\theta = (T - T_{inlet})/T_o$ where $T_o = T_w - T_{in}$ and St_{conv} and St_{rad} are the convective and radiative Stokes numbers defined as

$$St_{conv} = \frac{\tau_{conv,p}}{\tau_f} = \frac{\frac{\rho_p c_p D_p}{6h}}{\frac{D}{u_{max}}} \quad 2\text{-}16$$

$$St_{rad} = \frac{\tau_{rad,p}}{\tau_f} = \frac{\frac{\rho_p c_p D_p}{6h_r}}{\frac{D}{u_{max}}} \quad 2\text{-}17$$

respectively, where $h_r = \epsilon\sigma(T_p + T_w) * (T_p^2 + T_w^2)$. These thermal Stokes numbers are a measure of how quickly the particle temperature reacts to the surrounding carrier phase heat transfer mechanism and are analogous to the momentum Stokes number. In Equation 2-15, the importance of convection and radiation to particle heat transfer is reflected in the relative magnitude of their Stokes numbers – the mode with the smaller Stokes number has the larger influence on particle heat transfer. Note that T_o depends on the boundary conditions used for the problem.

When a wall collision occurs the particle temperature is compared to the particle softening temperature, T_{ST}, to characterize deposition on the surface. If a particle impacts the surface with a temperature higher than T_{ST}, it is deposited on the surface and removed from the calculation. On the other hand, if on impact the particle temperature is below the softening temperature then the particle bounces off the wall assuming an elastic collision. Other factors such as surface roughness, previous deposition, etc. are not considered in the deposition criteria and could potentially play an important role in the long term behavior of deposition growth.

Chapter 3
Validation

Since the flow field is the dominant factor into the characteristics of the particle's behavior, proper resolution of the flow field is key. To ensure this, the code and solver must be validated versus available experimental data to lend confidence to the fluid solution accuracy. A short pin fin array under a fully developed assumption will be used to compare to previous experiments.

3.1 Validation Geometry

The basis for the validation case geometry will be based off the work of Meztger [2-4]. Figure 3-1 gives the geometry as used in Metzger's experiments. The streamwise and spanwise pin spacings are 1.5D and 2.5D respectively from pin center to center, where D is the pin diameter. This gives a diagonal pin spacing (W/D) of 1.95. Note that walls exist at the y = 0 and y = H, where H is the pin height. The ratio of pin height, H, to pin diameter, D is 1 (H/D =1).

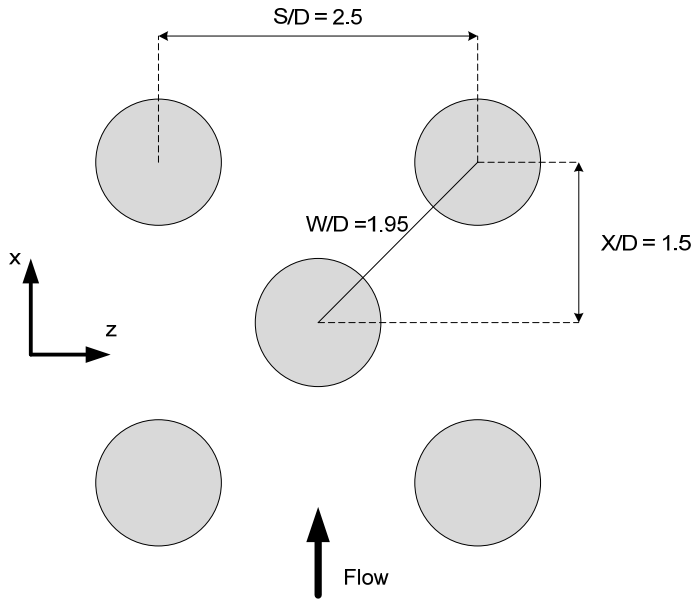

Figure 3-1: Geometry used by Meztger for pin fin studies[2]

Figure 3-2 shows the validation computational domain. Notice the domain consists of two full pin rows in both the streamwise and spanwise direction. In order to create a fully developed fluid field, the inlet and outlet boundaries (x-direction) are assumed periodic with each other. The left and right boundaries (z-direction) of the domain are also made periodic to create an infinitely wide domain in the spanwise direction. Thermally, a constant heat flux condition is used on all surfaces. A mesh of approximately 2.2 million cells is then applied to the domain. The mesh size for validation will be proved sufficient through a grid independency study in Section 4.2.

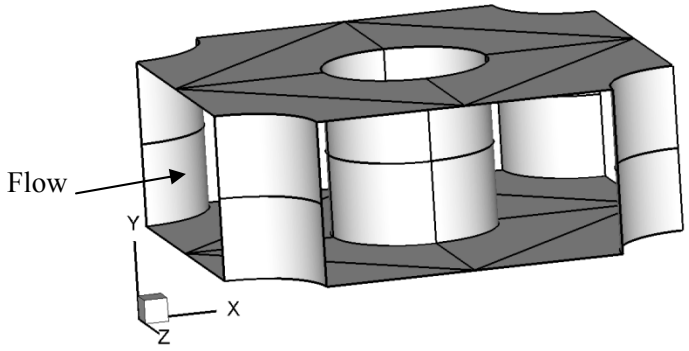

Figure 3-2: Fully developed computation domain

3.2 Fully Developed Assumption

The computations are conducted under the assumption of fully developed flow and heat transfer. Essentially this means that that every period of the domain is identical in terms of the flow and thermal structure. To achieve this, the inlet and outlet of the domain are coupled by a periodic condition. This presents no problems for most of the flow parameters, namely the velocity components. However if the velocity is to be the same entering and exiting the domain, then there must be a pressure gradient across the domain to drive the flow. Under a fully developed assumption, this pressure drop would be constant. A similar argument can be made for temperature change in the domain. To account for this, the pressure

and temperature fields are decomposed into periodically varying and spatially constant gradient components. In dimensional terms, these are

$$P(x,t) = P_{ref}(x,t) - \beta x + p(x,t) \quad 3\text{-}1$$

$$T(x,t) = T_{ref} + \gamma x + \phi(x,t) \quad 3\text{-}2$$

where $\beta = -\Delta P_x/L_x$ is the average pressure drop in the streamwise direction with L_x being the length of the domain in the streamwise (x) direction, p is the periodic pressure fluctuation, γ is the mean temperature gradient and ϕ is the periodic temperature fluctuations. Under the fully developed assumption, the friction velocity, u_τ, will be used as the reference velocity. The friction velocity is defined as

$$u_{ref} = u_\tau = \sqrt{\frac{\tau_{eq}}{\rho}} \quad 3\text{-}3$$

where τ_{eq} is the equivalent wall shear stress. This stress is an equivalent wall shear stress that includes both the form and friction losses of the domain. Using a mean momentum balance, the friction velocity can be defined

$$u_{ref} = u_\tau = \sqrt{\frac{\tau_{eq}}{\rho}} = \sqrt{\left(-\frac{\Delta P_x}{L_x}\right)\left(\frac{D_H}{4\rho}\right)} \quad 3\text{-}4$$

where D_H is the hydraulic diameter. This formulation also requires a specific T_o. At walls, a constant heat flux condition is applied, thus

$$T_o = \frac{q_w L_{ref}}{k} \quad 3\text{-}5$$

defined as the characteristic temperature, where $-q_w$ is the applied heat flux at the walls. Non-dimensionalizing Equations 3-1 and 3-2 using the appropriate non-dimensionalization parameters as given above yields

$$P^*(x,t) = -\beta^* x + p^*(x,t) \quad 3\text{-}6$$

$$\theta(x,t) = \gamma^*(t)x + \phi^*(x,t) \tag{3-7}$$

β^* is set equal to 1.

The momentum and energy equations can now be modified to account for these changes and are given as

$$\frac{\partial u^*}{\partial t^*} + \vec{\nabla}\cdot\left(\overrightarrow{u^*}\,\overrightarrow{u^*}\right) = -\nabla p^* + \vec{\nabla}\cdot\left(\left(\frac{1}{Re_\tau} + \frac{1}{Re_{\tau,t}}\right)\vec{\nabla}\overrightarrow{u^*}\right) + \beta^*\overrightarrow{e_x} \tag{3-8}$$

$$\frac{\partial \theta}{\partial t^*} + \vec{\nabla}\cdot\left(\overrightarrow{u^*}\theta\right) = \vec{\nabla}\cdot\left(\left(\frac{1}{Re_\tau\, Pr} + \frac{1}{Re_{\tau,t}Pr_t}\right)\vec{\nabla}\theta\right) - \gamma^* u_x^* \tag{3-9}$$

The Reynolds number based on friction velocity, Re_τ, is given as an input to the simulation. The flow field is then allowed to develop using this fact and β^* =1. To achieve the desired flowrate some iteration is required.

The non-dimensional temperature gradient, γ^*, can be given in a quasi-steady formulation as

$$\gamma^* = \frac{\Omega_S^*}{RePrQ_x^*L_x^*} = \frac{A_w^*}{RePrQ_x^*L_x^*} \tag{3-10}$$

where Ω_S^* is the non-dimensional heat transfer area and is equivalent to the total wall area, A_w^*, since the heat flux is applied over all wall surfaces in the domain. Q_x^* is the non-dimensional flow rate in the streamwise direction. Tafti [19] showed for problems without extreme unsteadiness that the above formulation for γ^* is adequate. For all fully-developed heat transfer cases, the non-dimensional heat flux, q_w^*, is set to a constant value of 1. The preceding formulation now provides for a periodic fully developed assumption to the flow field.

3.3 Fully Developed Flow Data Reduction

The method of calculation of the various fluid and thermal parameters is very important, especially when comparing to experimental values. The first parameter needed is the Reynolds number based on the

pin diameter and u_{max}. Under the fully developed assumption, the Reynolds number within the solver is defined using the friction velocity and is designated as Re_τ. Note that pin diameter is used as the reference length in all formulations of Reynolds number. To determine the Reynolds number based on u_{max} the following relation is used

$$\frac{Re}{Re_\tau} = \frac{u^*_{max}}{u^*_\tau} = \frac{Q^*_x}{A^*_{min}} \tag{3-11}$$

where $u^*_\tau = 1$. Since, the flowrate is a consequence of a pressure gradient and is not precisely set; some iteration is required to achieve the desired Reynolds number.

The friction factor, f, is an important parameter to characterize the penalty required to maintain the flow field. The friction factor as defined by Metzger [3] is

$$f = \frac{\Delta P}{2\rho u^2_{max} N}. \tag{3-12}$$

where N is the number of pin rows. This can be formulated non-dimensionally as

$$f = \frac{\Delta P}{2\rho u^2_{max} N} = \frac{\left(\frac{\Delta P^*}{L^*_x}\right) L^*_x}{2 {u^*_{max}}^2 N} = \frac{L^*_x}{2 {u^*_{max}}^2 N} \tag{3-13}$$

Noting that $\left(\frac{\Delta P^*}{L^*_x}\right) = \beta^*$ which is set to a value of 1.

The final parameter is the Nusselt number. The Nusselt number is defined as

$$Nu = \frac{hL_{ref}}{k} \tag{3-14}$$

The heat transfer coefficient h is then defined as

$$h = \frac{q_w}{T_w - T_{bulk}} \tag{3-15}$$

where T_w is the local surface temperature and T_{bulk} is the bulk mean temperature of the domain. Plugging in the expression for h into the Nusselt number formulation and non-dimensionalizing all the terms yields

$$Nu = \frac{q_w^*}{\theta_w - \theta_{bulk}} = \frac{1}{\theta_w - \theta_{bulk}} \tag{3-16}$$

The non-dimensional bulk temperature can be found through a volume integration as

$$\theta_{bulk} = \frac{\int_{L_x^*} \iint \theta |u| \, dy^* dz^* dx^*}{\int_{L_x^*} \iint |u| \, dy^* dz^* dx^*} \tag{3-17}$$

The average Nusselt number can also be found using Equation 3-16. The area averaged surface temperature is used for θ_w along with the time-averaged θ_{bulk} to find the average Nusselt number.

3.4 Fluid and Thermal Results

The work of Metzger et al. [2-4] will be the main basis for comparison of the computational and experimental results. The simulation was run at varying Reynolds numbers (Re) based on u_{max} and the pin diameter, ranging from approximately 2500 to 10,000. Note u_{max} is the velocity at the streamwise minimum area, A_{min}. At each Reynolds number, the flow is allowed to develop and then averaged in time. Within this region two Reynolds numbers (3980 and 7310) are matched within a few percent to allow for direct comparison to Metzger. The other Reynolds numbers are used to create a comparison of the trends to the experiments.

The first point of comparison will be the friction factor, f. Note that within the framework of the fully developed simulation the ΔP is fixed and the flow is allowed to develop from this fixed value (See

Section 3.2 for details). In the experiments, the u_{max} is fixed by setting the mass flow rate and the pressure is then measured with static pressure probes at the walls. Figure 3-3 shows how the simulation compares to the correlation derived by Metzger et al. [2]. Armstrong and Winstanley [5] note that the correlation fits the available experimental data within 15%. All values from the simulation fit within 15% of the correlation except the first two values which were 20% and 16 % respectively. Also, the simulation to correlation fit improves with higher Reynolds number. One cause of this discrepancy may lie in how the pressure values are measured. In GenIDLEST, the friction factor is calculated using averaged quantities for u_{max} at the inlet plane. Note that since the pressure gradient is constant, it is the u_{max} that varies. In the experiments, the pressure drop over the array is measured in one (or several) location(s) (namely at the wall end walls). These different measurement methods could lead to differences between the experiment and simulation. Despite the slight over prediction, the trend between the simulation and correlation matches quite well.

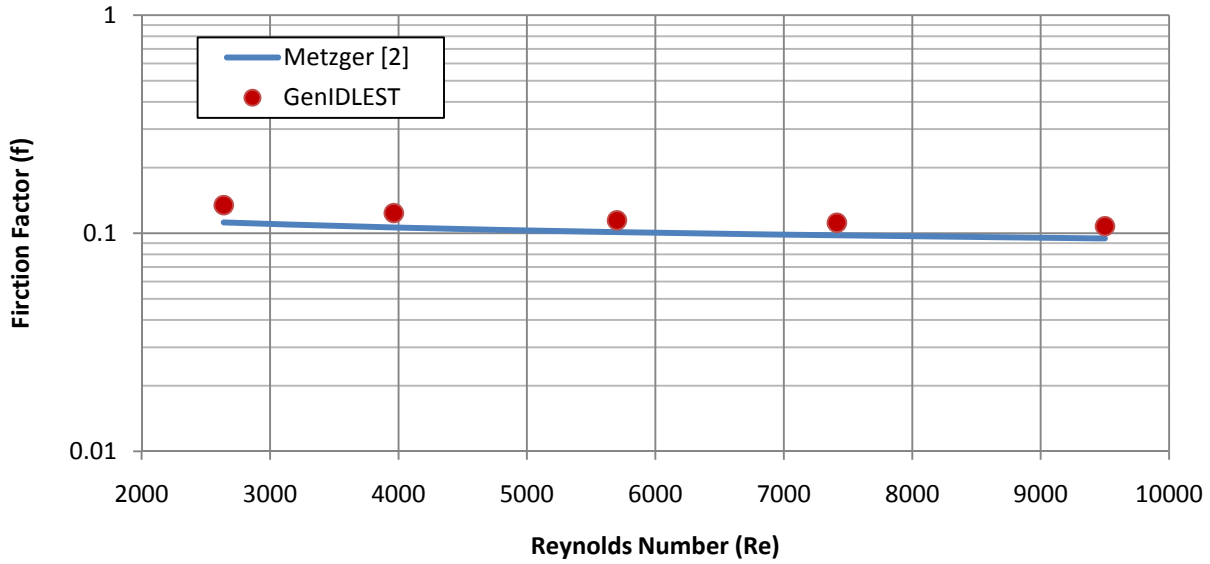

Figure 3-3: Comparison of f versus Re

Other important parameters within a pin fin array are the heat transfer characteristics. For the pin fin arrays, this can be represented by the average and row resolved Nusselt numbers

($\overline{Nu}$ and Nu respectively). Note that almost all experiments on short pin fin arrays have been of a developing nature. Thus to match the fully developed nature of the simulation, the experimental comparison data is taken at the 7th pin row where the flow is fully developed. The 7th row was chosen since the flow is shown to be developed, while further downstream, the end effects of the pin fin array may become prominent. The experimental data from Metzger et al. [2] is used to capture the 7^{th} row Nusselt number for the various Reynolds numbers. Figure 3-4 shows Nusselt number versus Reynolds number for both the simulation and the experiments. Only four experimental points are viable from within the Reynolds number range covered. The Reynolds numbers of 3980 and 7310 are the two direct comparison points between the experiments and simulation. At Re = 3980, the simulation and experiments are in close agreement with an approximate 5% difference which is within experimental uncertainty. At Re = 7310, the simulation over predicts by approximately 13% when corrected for the slight Reynolds number differences between the simulation and experiment. The overall trend between experiments and simulations is quite close with the Reynolds number power dependence being 0.7013 and 0.6764 respectively for the seventh row Nusselt number. Note that Chyu [7] found an exponent of 0.58 for the array averaged Nusselt number compared to Meztger's [2] 0.685. Thus, the difference between simulation and experiments is well within the range expected.

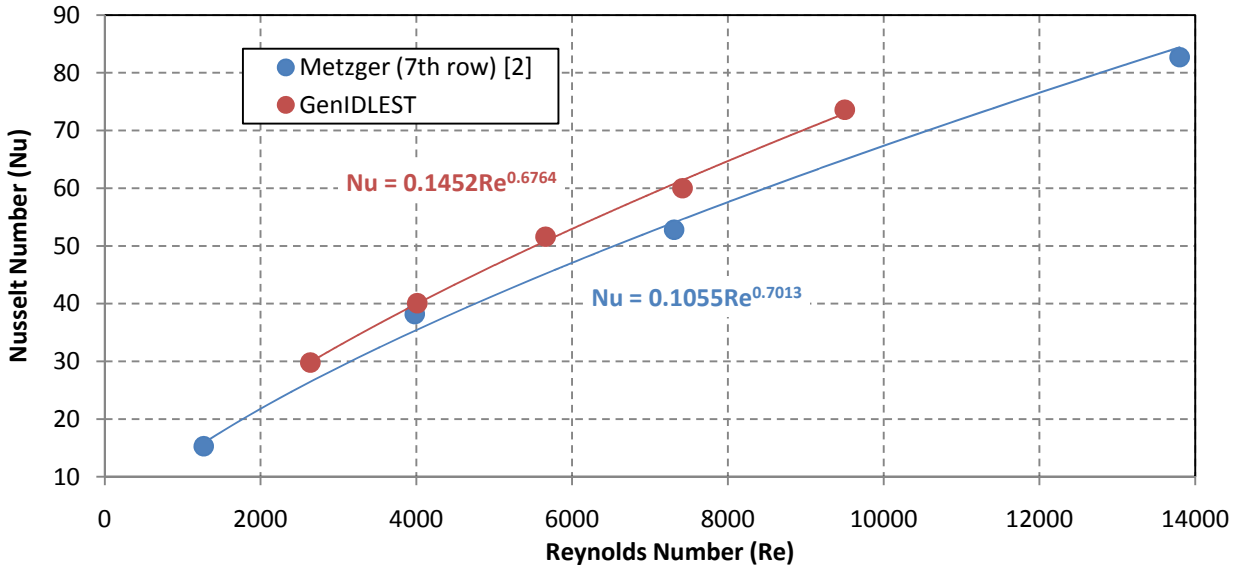

Figure 3-4: Comparison of Nusselt number (Nu) versus Reynolds number (Re)

Overall, the simulations appear to match the trends of correlations and experiments well. There is some over prediction in both Nusselt number and the friction factor. For the Nusselt number, discrepancies between the thermal boundary conditions and methods of calculation between the simulation and experiment may be the cause of the different values. In the simulations, a constant heat flux condition is applied to the pins and end walls. In Metzger's experiments an isothermal condition is assumed, however, only 4 thermocouples are used to sample the temperature at the channel (endwall) surface at each pin row. The validity of using these endwalls temperatures at the pin faces is questionable, especially with increasing Reynolds number. The current simulations show that Nusselt number is higher on the pins and thus the wall temperature at the pins must be lower than the end walls. Also since Metzger's experiments were ran with low temperature differences, a small deviation from the constant temperature condition can result in significant changes in Nusselt number. Chyu et al. [7] back this by noting how difficult perfect thermal boundary conditions in experiments can be to obtain and how the results can then be affected. They state that the inaccuracies in the heat transfer quantities would be significant at the row resolved

level where the pin area is significant. However, the total average over the array may be relatively unaffected due to the large total wall area where the boundary conditions are closer to the assumed boundary conditions. Chyu also notes that the trends in Nusselt number are relatively insensitive to the measurement technique and boundary conditions while the actual magnitudes are not. The simulations match all trends very well and the magnitudes, while over predicted, are still considerably close to the experimental values given the possible inaccuracies. This and other grid independency studies (Section 4.2) lend confidence to the accuracy of the simulations.

Chapter 4

Sand Particle Transport within a Fully Developed Pin Fin Array

The purpose of this chapter is to give an introduction to the final pin fin array geometry and investigate the basic particle behavior within a pin fin array. The previous chapter showed that the solver gives accurate results for a short pin fin array. This chapter will describe the geometry of the pin fin array as well as investigate the grid independency of the simulation. The fluid and thermal fields will then be detailed before finally injecting particles to investigate their behavior.

4.1 Geometry and Grid

The basis for the current geometry is the channel with pin-fins as used in the validation case. Figure 4-1 shows a top view of the geometry. Again, the height of the channel is taken to be equivalent to the diameter of the pin, H/D = 1. However, the streamwise and spanwise pitches are now 1.414D and 2.828D, respectively, where D is still the diameter of the pin. This is a 5.7% decrease and 13% increase in streamwise and spanwise spacing respectively. Thus, the geometry is still close to the validation case geometry. Note that there are walls on the top and bottom of the geometry at y = 0 and y = H. The flow is taken in the positive x-direction. From here, a domain is built exactly as the validation case but with the modified pin spacing.

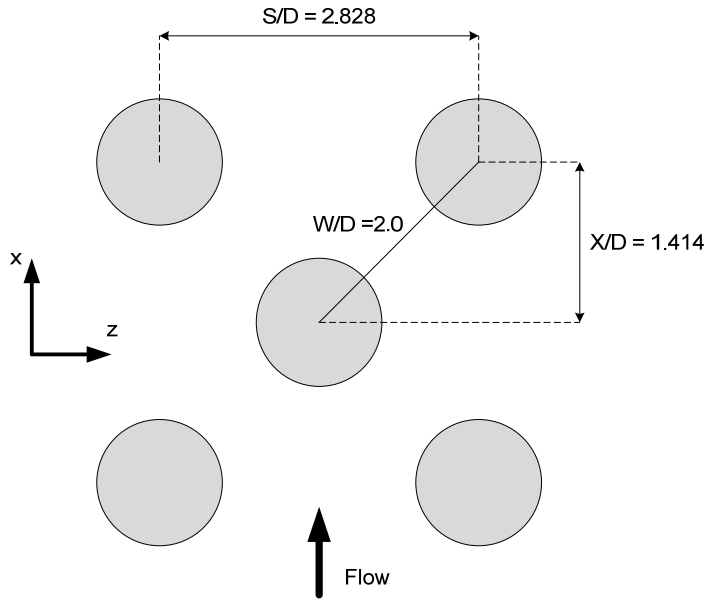

Figure 4-1: Top view of pin fin array layout

4.2 Grid Independency

Three different mesh sizes (fine, coarse, very coarse) are chosen with an approximate factor of 2 difference in the total number of cells between each mesh (2.2 million, 1.15 million, 0.57 million). All studies are conducted at a nominal Reynolds number (Re) of 9700, based on the velocity at minimum area (u_{max}) and the pin diameter (D). Each calculation consists of an initial "development time" in which the flow adjusts to the applied pressure gradient to produce a statistically stationary state of turbulence, after which it is time averaged to obtain the mean flow and heat transfer parameters. Table 4-1 shows the time-averaged results of the grid independency study. In going from the fine to coarse mesh, the percentage difference is only 2.2% for the mean maximum velocities, u_{max}. The friction factor has a somewhat larger error since it is a function of the velocity squared. The Nusselt number (Nu) shows an approximately 1-1.5% increase when coarsening the mesh. This is to be expected since the increased flowrate will increase Reynolds number and thus Nusselt number. Using this result and investigating the time needed to run the

calculations, the fine mesh was chosen as it gives the best accuracy with an acceptable penalty as far as total computation time.

Table 4-1: Grid dependency results for the three mesh sizes

Parameters	Fine	Coarse	%-Diff-Coarse	Very Coarse	%-Diff-Very Coarse
Number of Cells x 10^{-6}	2.21	1.15	-	0.57	-
Flow Rate	4.95	5.06	2.3	5.21	5.3
u^*_{max}	2.71	2.77	2.2	2.85	5.2
Re	9752	9972	2.3	10264	5.3
f	0.098	0.092	6.1	0.087	11.2
Nu	77.8	78.6	1.0	78.9	1.4

4.3 Flow Results

The simulation was allowed to run until the solution had reached a "steady" or stationary state. After this state is reached, the results are averaged over time to obtain the mean quantities. The time averaging for the fully developed simulation is over 8 non-dimensional time units. The non-dimensional u^* velocity contours can be seen for two slices in Figure 4-2 for a Re of 9700. Note that u_{max} is used as the reference velocity. The first slice is taken at the centerline ($y^* = 0.50$) of the pin fin array. The fluid shows acceleration around the pin peaking at about a surface angle of approximately 81° around the pin. The front of the pin shows a stagnation region with a wake region behind the pin. The second slice is taken near the wall ($y^* = 0.02$). Overall the effect of the wall has lessened the magnitude of the velocity. Now present in front of the pins is a horseshoe vortex caused by the interaction of the pin and the wall. The strength of the vortex is quite strong with reversed flow magnitude reaching approximately 30% of the u_{max} velocity. The f at this Re is calculated to be 0.098. This compares well with Meztger's correlation for f which is applicable since Meztger and Haley [4] showed that f is relatively insensitive to the streamwise spacing (X/D).

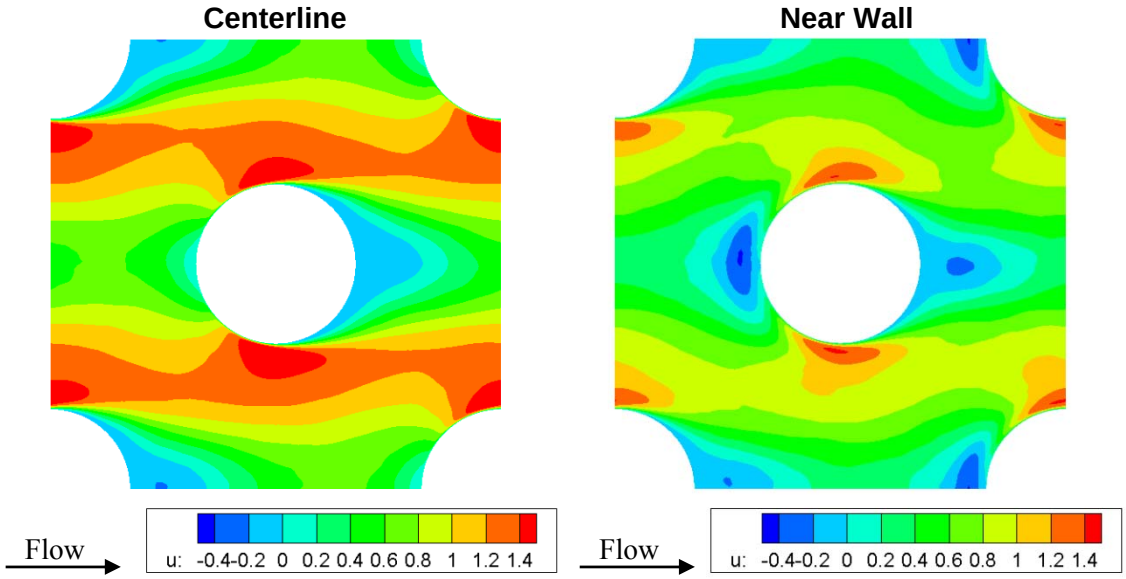

Figure 4-2: u^* velocity contours at centerline and near wall

4.4 Heat Transfer Results

Several values of Reynolds number ranging from 2500-13,000 were tested to see how the thermal results compare with those of the experiments and the validation geometry. Figure 4-3 shows Nusselt number versus Reynolds number trend for the current case as well as the validation and experimental cases. Throughout the Reynolds number span the X/D = 1.414 case has a higher Nusselt number, which is to be expected. The tighter streamwise spacing increases the turbulence levels resulting in increased heat transfer. The Reynolds number dependence is very close to the validation case with 0.6594 and 0.6764 for the current and validation cases respectively. Figure 4-4 shows the Nusselt number normalized by the square root of Reynolds number at the centerline and near wall of the pin for varying surface angles (0° is stagnation). The Reynolds number in Figure 4-4 is 9700. The plot shows that the centerline peak heat transfer occurs in the stagnation region. The minimum heat transfer occurs near separation at 103° around the pin and remains low in most of the wake till it increases slightly in the rear stagnation region as the recirculating wake impinges on the pin. In the near wall plot, the Nu is fairly low throughout the pin surface with a peak at stagnation and a reduced value in the wake region. Zhu et al. [28] in their

investigation of pin fin arrays noted that the heat transfer on the pin was lowest in the region bounded by the horseshoe vortex near the walls. The current simulation sees this as well. Zhu et al. also see the maximum heat transfer on the channel (endwall) in the region in front of the pin where the horseshoe vortex appears with a magnitude close to that of the heat transfer on the pin face. This is also seen in the current simulation.

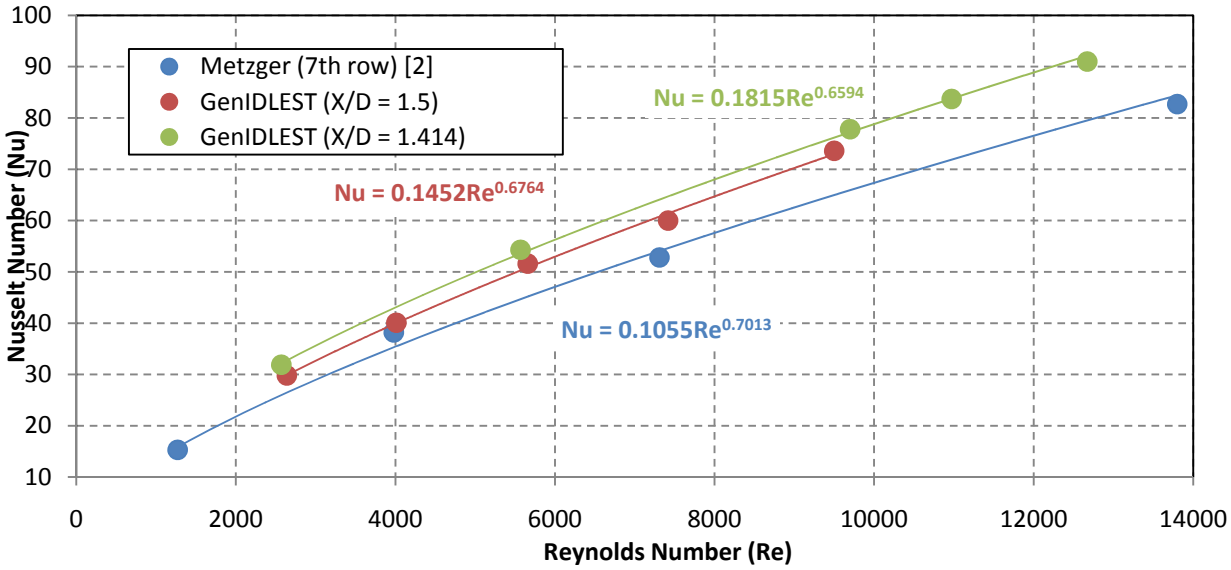

Figure 4-3: Nu versus Re for GenIDLEST with X/D 1.5, X/D= 1.414 and Metzger [2]

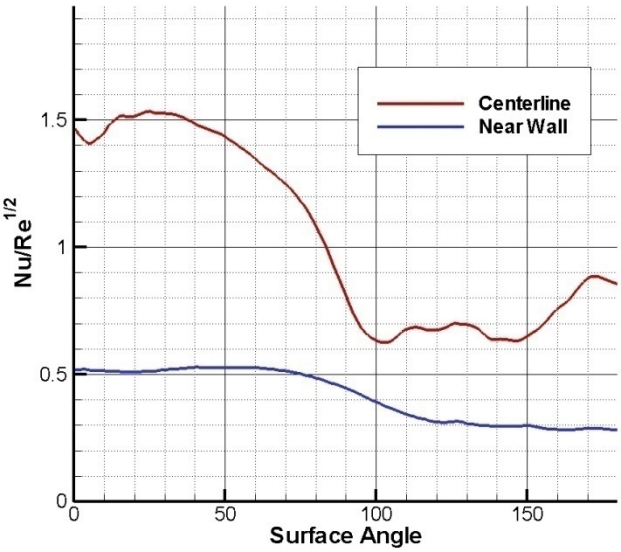

Figure 4-4: $Nu/Re^{1/2}$ versus surface angle for the centerline and near wall of the pin. (Re = 9700)

4.5 Particle Transport in Fully Developed Flow

To develop an understanding of the particle behavior in the pin fin array, an initial calculation is performed using the fully developed fluid field. Two different particle sizes yielding Stokes number (St_p) of 0.38 and 9.62 are investigated.

4.5.1 Force Magnitude Analysis

Before looking into the deposition and collision characteristics, a single particle is injected and tracked to estimate the forces and validate the use of only the drag force. All forces including drag, added mass, lift, pressure, Brownian and Bassett are applied to the particle. These forces are then sampled every few time steps to determine if the assumption of drag being the dominant force is valid. Both Stokes numbers are investigated at two different initial locations, channel center and near wall. Figure 4-5 shows the averaged force magnitudes normalized by drag for the different scenarios. In all scenarios the Brownian, Bassett, added mass and pressure forces are at least one order of magnitude less than the drag force. At the center of the channel, the lift force is approximately one order of magnitude lower than the drag force.

As expected, near wall the lift force increases in magnitude. For the $St_p = 0.38$ particles, the magnitude is approximately 20% of the drag force. For the $St_p = 9.62$, the lift force's magnitude is even greater at 46%. Note however that these particles are injected near the channel wall. For particles that enter the near wall region from the center of the channel, their momentum will very quickly carry them toward the wall and then back out after collision. This is especially true for the higher Stokes number particles. Thus, the assumption that drag is the dominant force is valid for the given particles and flow conditions.

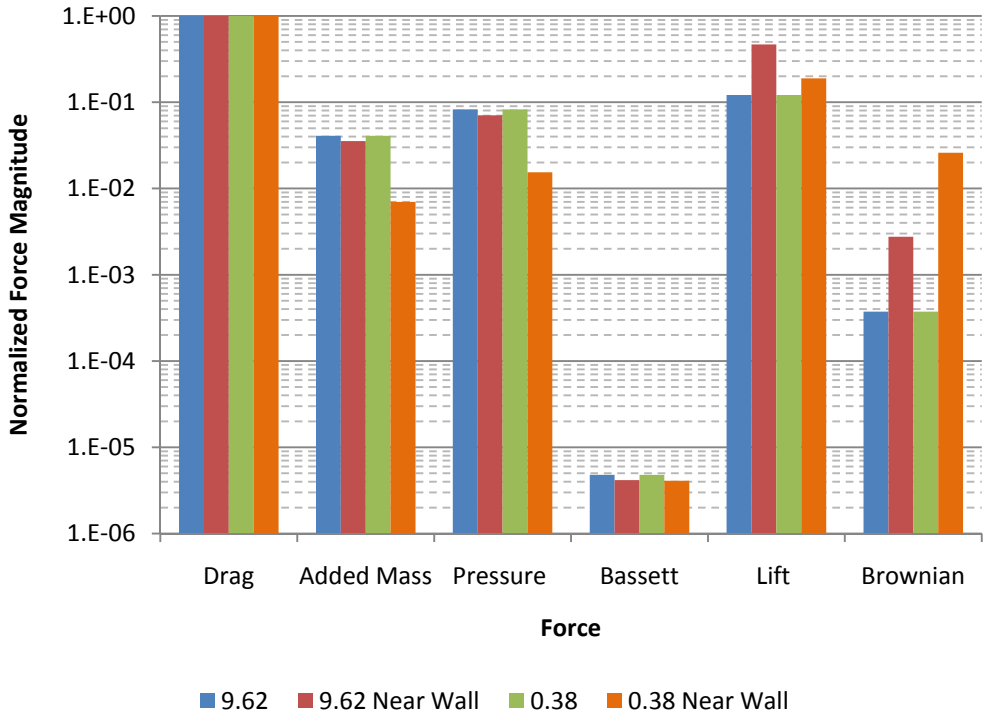

Figure 4-5: Comparison of magnitudes for the different forces acting on the particles for two stokes numbers and two initial locations

4.5.2 Particle Deposition

The fully developed domain will be used to obtain an understanding of how the particles deposit and how long they stay in the pin fin array. To accomplish this, the number of times a particle crossed the streamwise periodic boundary is recorded. The particle's deposition location can then be determined by adjusting the particle's current deposition location by the number of traverses through the domain the

particle has completed. This allows for the tracking of the particles as if they were within a larger domain while only calculating them in the fully developed two-row domain. Also, the deposition model is simplified to assume that any collision with a surface results in the particle depositing on that surface irrespective of the state of the particle. This assumption would simulate the worst case scenario as far as particle deposition is concerned. The calculation was initialized by placing 10,000 particles in the core domain (assuming the local fluid velocity) and integrating for an initial time period in which no particles were allowed to deposit on the surfaces but instead bounced back through elastic collisions. This was necessary to have the particles reach their natural or steady state in the flow field. After this, the deposition model was activated such that any particle impinging on a surface was recorded as a deposit and the particle removed from the calculation.

The higher Stokes number particles are more likely to impact on the pin surfaces than the lower Stokes number particles. Figure 4-6 shows the distribution of deposits for the $St_p = 9.62$ particles. In the side view, it is seen that the particles mostly deposit on the frontal projected area of the pins. As the particles travel along (recorded through number of traverses out of the core domain), the number of deposits decreases as the number of available particles decreases. Of note here is that the particles only deposit on the frontal projected part of the pin. This is due to their inability to follow the flow into the wake region. This inability to follow streamlines into the wake is also shown top view in that depositions along the channel walls are absent within the wake regions. This is not true in the first row due to the fact that the first row contains particles from the initialization period.

The $St_p = 0.38$ particles show different deposition characteristics than the $St_p = 9.62$ particles. Figure 4-7 shows the deposits for the $St_p = 0.38$ particles. While the majority of the particles still deposit on the pins, the density of deposition is less, particularly along the sides of the pin. This is due to the fact that the $St_p = 0.38$ particles are able to better follow the main stream flow around the pin instead of impacting the pin. For the same reason, the wake regions of the pins are also more populated. Another major difference

between the two particle sizes is that the $St_p = 0.38$ particles have many more depositions along the walls of the channel.

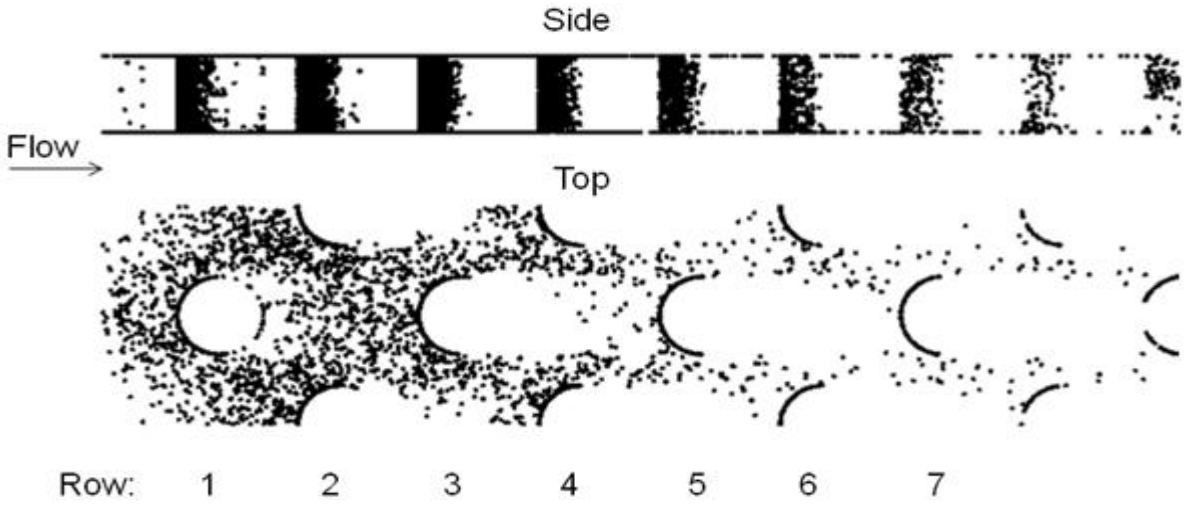

Figure 4-6: Simulated $St_p = 9.62$ deposits using the number of traverses in the flow direction

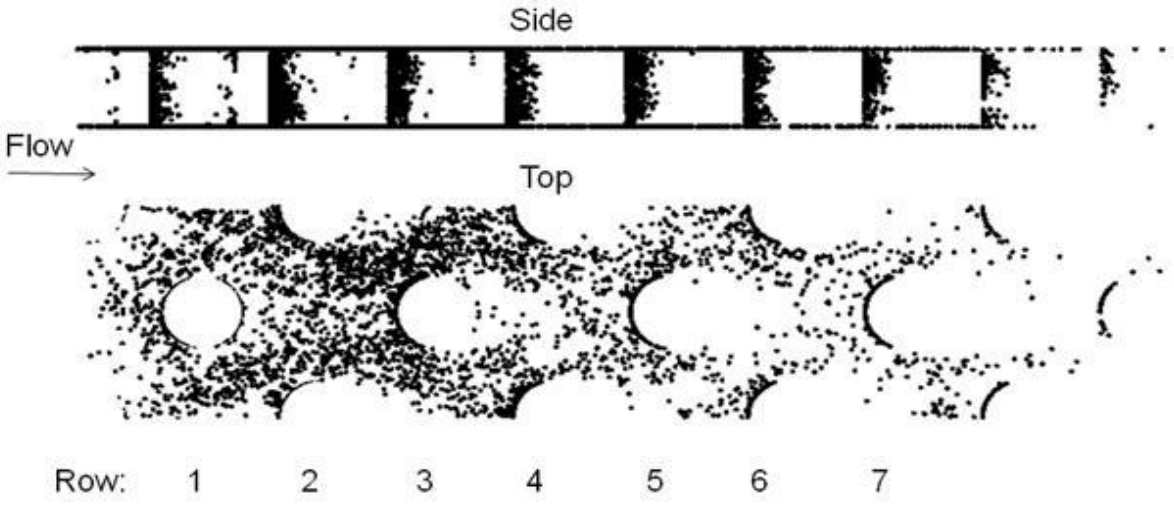

Figure 4-7: Simulated $St_p = 0.38$ deposits using the number of traverses in the flow direction

Figure 4-8 shows the percentage of total deposited particles for each domain traverse. For both particle sizes, a majority of the particle deposits are within the first two traverses. By the fourth traverse, the end of the developing flow geometry used in Chapter 5, 97% of all the $St_p = 9.6$ and 85% of all the $St_p = 0.38$ micron particles have been deposited. Another interesting statistic is the number of particles that are

deposited on the pins versus the channel walls. St_p = 9.6 particles have 78% of their deposits on pins; while the St_p = 0.38 particles have 54% deposited particles deposit on pins.

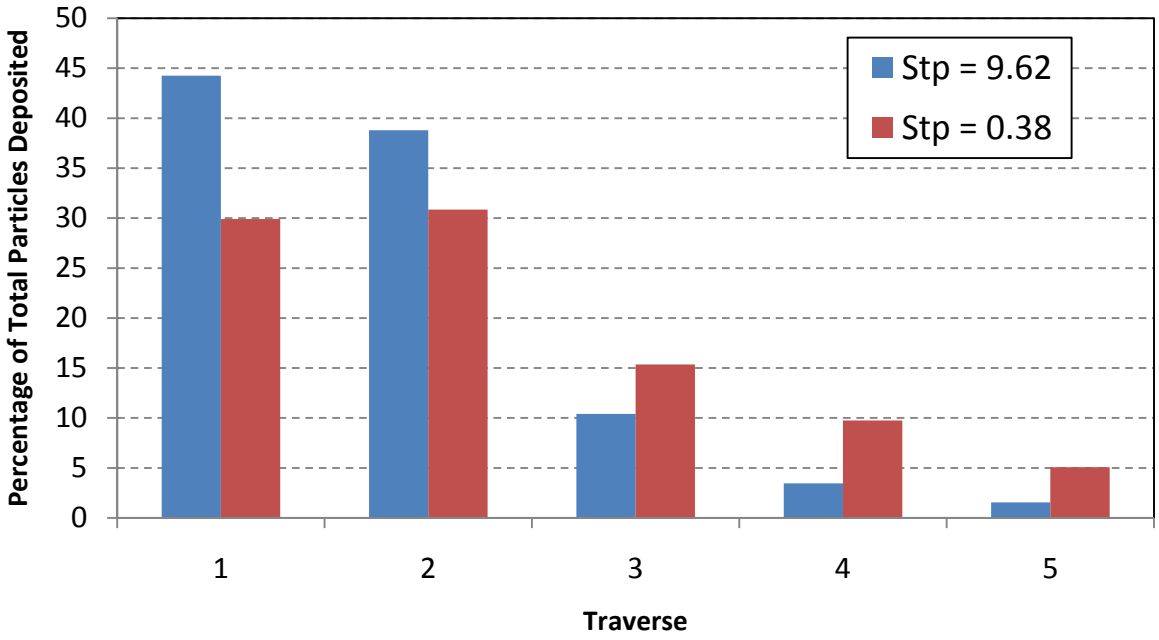

Figure 4-8: Percentage of total deposited particles versus traverse

Since the flow field is fully developed, the particles should exhibit a similar fully developed behavior in the percentage deposition. Figure 4-9 shows the normalized deposition percentage versus traverse. The deposition is normalized by the incoming particles to the current traverse, not the total number of particles injected. Under a fully developed assumption, this percentage should be approximately constant. For the St_p = 0.38 particles, the percentage is relatively constant for traverses two through five. After this, so many particles have deposited that the sample size is too small to give statistically accurate results. The St_p = 9.82 particles percentage is only constant in traverses four and five. Again, in later rows the sample size is too small to give accurate results. The non-constant values for the St_p = 9.82 particles in the early traverses may be due to the particles not being fully developed as assumed. Due to the higher Stokes number the particles take much longer to adapt to the flow field and the initial integration time may not have been sufficient. The reason for the particles in the first two traverses being so different may also be

due to the fact that particles were not allowed to deposit during the initial integration. Since particles did not deposit during the initial integration time, some particles in the first traverse may have deposited in regions that normally would be void of particles, particularly behind the pins. If deposition had occurred during the integration time, these particles would not be in these regions and thus not deposit.

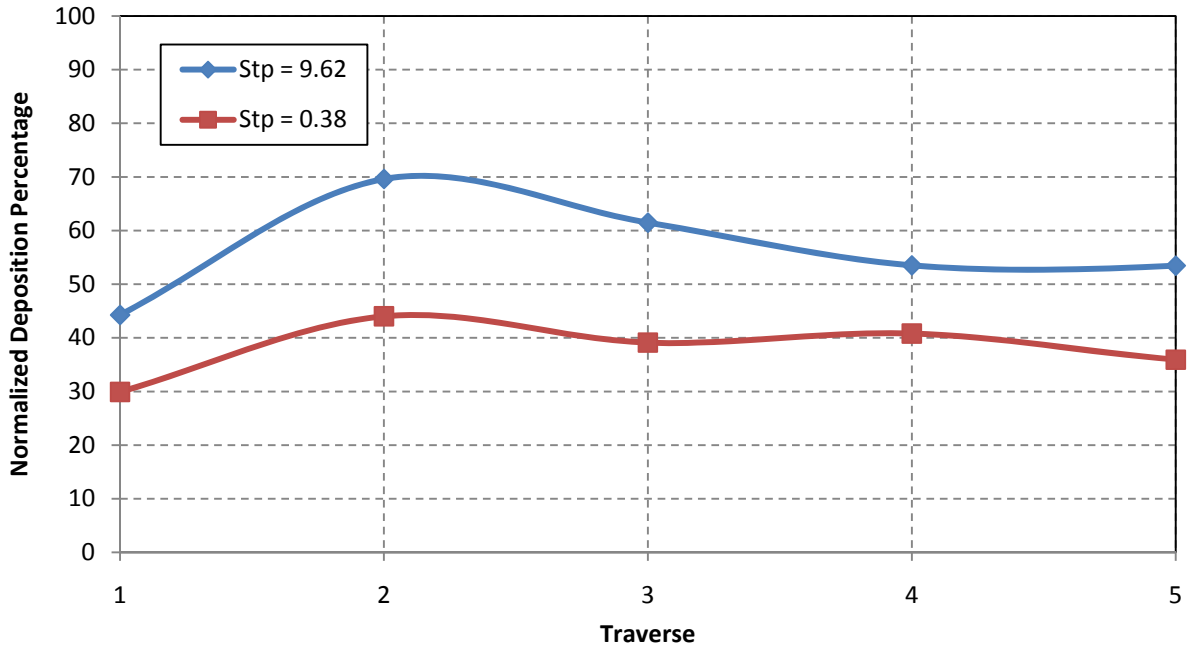

Figure 4-9: Normalized deposition percentage versus traverse number

Chapter 5

Sand Particle Transport within a Developing Pin Fin Array

In the previous chapters, we have validated the grid resolution and accuracy of the flow and heat transfer under a fully developed flow assumption. We also showed that the drag force is the dominant force acting on the particles and some of the basic particle characteristics within a pin fin array. This chapter will investigate particles within a developing pin fin array. The chapter will cover the geometry, the fluid and thermal results and finally investigate the particle behavior.

5.1 Geometry and Grid

The basis of the geometry will be the fully developed pin fin array created in Chapter 4. The fully developed geometry is repeated 3 times in the streamwise direction with an inlet and outlet section of 4D and 10D added to either end, respectively. Figure 5-1 shows this geometry and the flow direction with the top channel wall removed for clarity. Similar to the fully developed case, the spanwise direction will maintain periodicity allowing for a high aspect ratio pin fin array. However, the streamwise direction will be allowed to develop both hydrodynamically and thermally throughout the domain. The mesh is the same as the fully developed case. The channel and pin fins are maintained at a constant temperature (T_w).

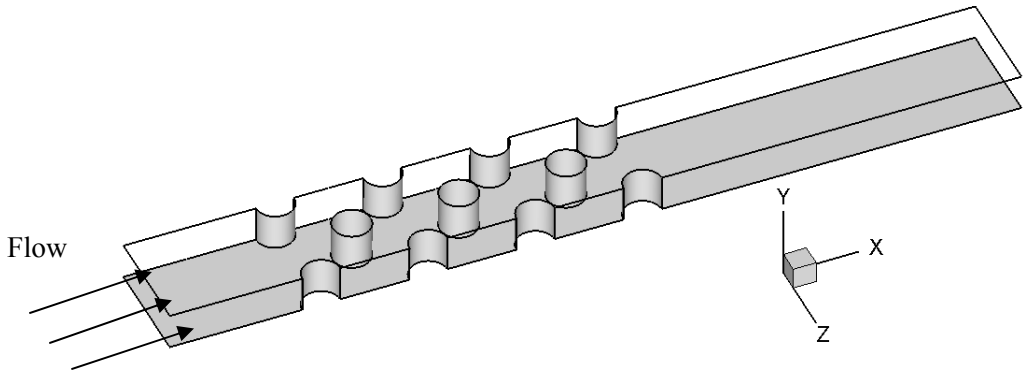

Figure 5-1: Full geometry layout

5.2 Developing Flow Data Reduction

The developing flow framework uses a more traditional approach to determine the fluid parameters as compared to the fully developed assumption. The fluid field is solved as described in Chapter 2 and requires no special treatment like the fully developed simulations do. Since a velocity in-flow condition is used, the Reynolds number can be precisely set using the continuity equation at the inlet and the A_{min} plane where u_{max} occurs. The friction factor is determined as before (See Equation **3-12**), by calculating the pressure drop via plane averaging just before and after the pin fin array. Also, the number of pin rows, N, has increased to 7.

Calculation of the Nusselt number is different from the fully developed simulations due to the constant temperature boundary condition. The Nusselt number is still calculated using Equation 3-16 given as

$$\mathrm{Nu} = \frac{q_w^*}{\theta_w - \theta_{bulk}} = \frac{q_w^*}{1 - \theta_{bulk}(x^*)} \qquad 5\text{-}1$$

Since the wall temperature is constant with $\theta_w = 1$, the denominator can be simplified as shown in Equation 5-1. The heat flux is now variable in both time and space and depends on the local conditions of the flow. The bulk temperature also increases due to the hot walls as the flow progresses through the pin fin array. To determine the bulk temperature profile as a function of the streamwise distance, planes are taken at various locations in the streamwise direction. The bulk temperature for the i^{th} plane is then found using

$$\theta_{bulk,i} = \frac{\iint_i \theta |u^*| dy^* dz^*}{\iint_i |u^*| dy^* dz^*} \qquad 5\text{-}2$$

A curve fit is then made over the plane-averaged bulk temperatures to describe how the bulk temperature changes in the streamwise direction. The local Nusselt number may then be calculated at each point. The average Nusselt number is found through an area average defined as

$$\overline{\mathrm{Nu}} = \frac{\iint \mathrm{Nu} dA^*}{A_w^*} \qquad 5\text{-}3$$

This formulation is applied for both the row-resolved and array averaged Nusselt numbers.

5.3 Flow and Thermal Results

The simulation was run at a Reynolds number of 15,470 based again on u_{max} and the pin diameter, D, from the initial state until a stationary flow state was established throughout the length of the channel. The data was then averaged in time to obtain the mean field. We first investigate the predicted structure of the flow field. The average u^*-velocity contours for $y^* = 0.50$ (centerline) and $y^* = 0.02$ (near wall) can be seen in Figure 5-2 and Figure 5-3, respectively. The first two rows exhibit a large wake region which shrinks in size as the flow becomes more turbulent further into the array. At the fourth pin row, the wake region has reached a constant size suggesting the flow is developed. Near the wall, the recirculating signature of the horseshoe vortex at the leading edge can be observed. Also, the areas of peak velocity reduce in size as the flow develops. The friction factor over the pin array was calculated to be 0.091 which is within ten percent of Metzger's correlation [3] for a pin fin array of similar geometry to the given pin fin array.

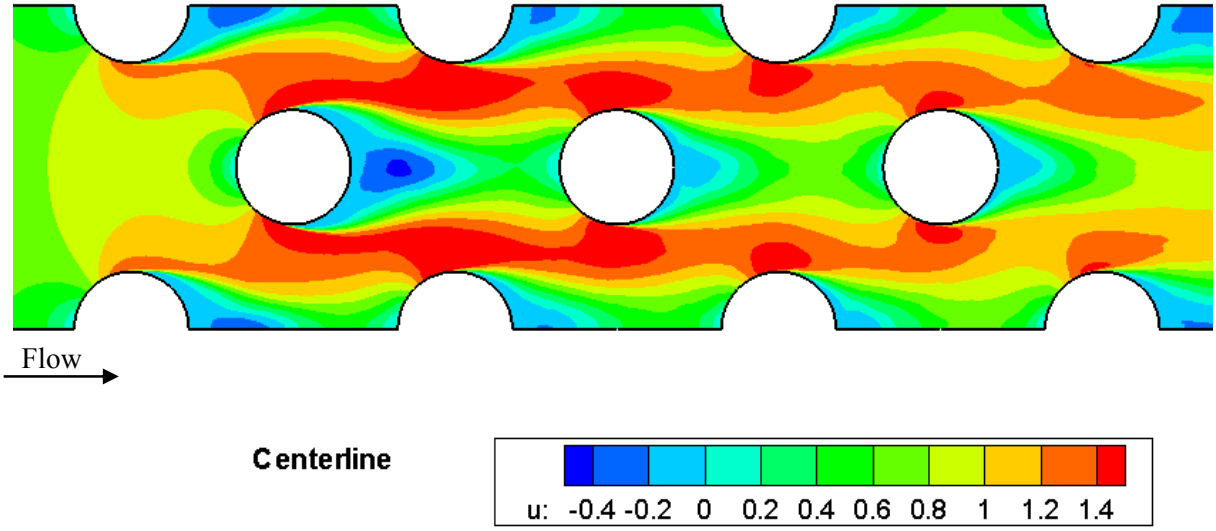

Figure 5-2: u^*-velocity contours plots at $y^* = 0.50$ for the developing flow

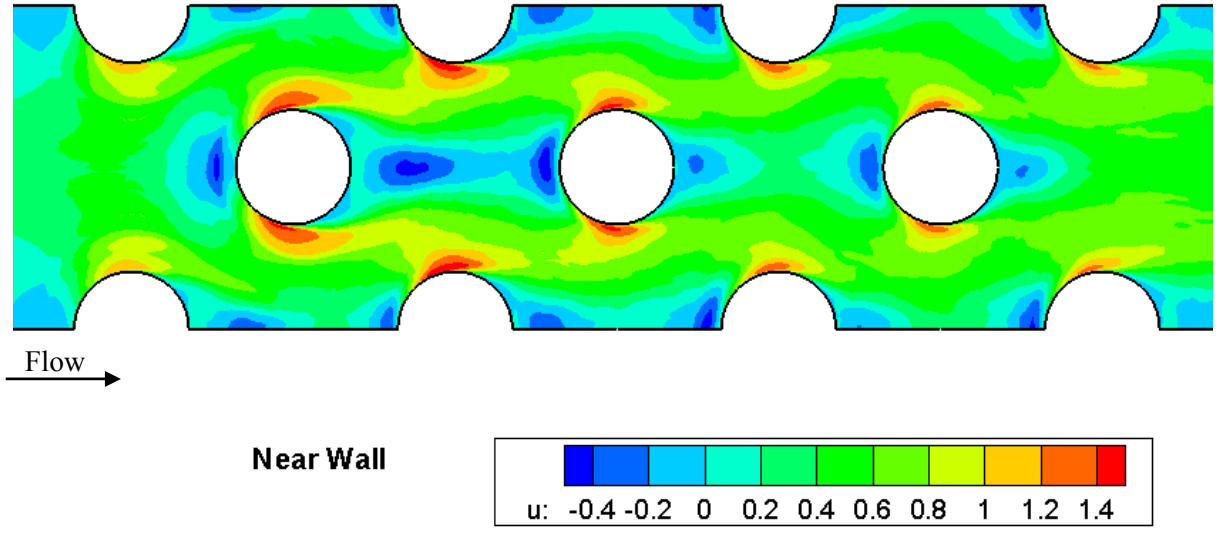

Figure 5-3: u^*-velocity contours plots at $y^* = 0.02$ for the developing flow

Turning now to the thermal characteristics of the flow, Figure 5-4 shows the distribution of normalized Reynolds numbers ($Nu/Re^{1/2}$) at the pin center versus angle around the pin where 0° is the stagnation point. In accordance with the work of Metzger and Haley [4] and Ames and Dvorak [8], this plot confirms

the trend that the Nusselt number is fully developed by the 4th row of pins. For all the rows, Nusselt number is highest at stagnation and has a minimum near the separation point. Also seen by previous experiments is the increase in heat transfer at the back of the pin which is seen here as well. The first two rows also show a significant increase, as compared to the later rows, in heat transfer almost to the same level as the front of the pin. This is also captured by Metzger and Haley [4] though no reason for this is given. One possible explanation for this is that the flow coming into the first two pins is laminar and the large coherent recirculating wake regions are successful in drawing in free stream fluid along the wake centerline which enhances heat transfer.

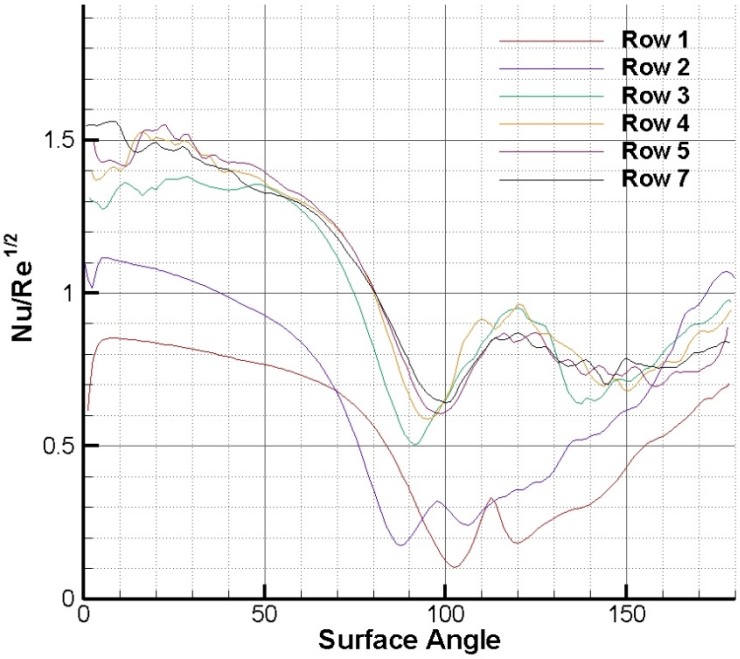

Figure 5-4: $Nu/Re^{1/2}$ versus surface angle at the pin centerline for the seven rows

Figure 5-5 shows the average Nusselt number for each pin row including the pin and channel walls. Nusselt number increases significantly until row 4, then rises slowly to row 5 where a maximum value is

reached before tapering off. This pattern is also seen by Metzger [2]. Metzger's experiments showed an increase in Nusselt number until the 4th or 5th row before a tapering off in latter rows. Metzger and Haley [4] state that the reason for the peak and subsequent taper is due to the peak turbulence intensity around the 4th row and then a slight reduction in later rows. The array averaged Nusselt number, $\overline{\mathrm{Nu}}$, for the pin fin array is 97.3. Meztger's array averaged Nusselt number ($\overline{\mathrm{Nu}}$) correlation [5] which accounts for the streamwise spacing differences is given as

$$\overline{\mathrm{Nu}} = 0.135\mathrm{Re}^{0.69}(\mathrm{X/D})^{-0.34}. \qquad 5\text{-}4$$

This correlation gives array averaged Nusselt number of 93.3, a difference of 4.3% which is within the experimental uncertainty. Note that the average value is much less dependent on the measurement technique and boundary condition assumptions as noted in Chapter 3. For the first row, the Nusselt number was found to be 53. Metzger's correlation for the Nusselt number of the first row [2] is given by

$$\mathrm{Nu} = 0.022\mathrm{Re}^{0.813}. \qquad 5\text{-}5$$

For the given Reynolds number, Metzger's correlation for the first pin row Nusselt number comes out to 56 with a difference of 5% with the simulation.

The fluid phase results compare well with the experimental trends and no major discrepancies are found. All data seems to suggest a fully developed region is established around or slightly after the 4th pin row. This is in agreement with experiments. A close match of the first row Nusselt number (Nu) and the array averaged Nusselt number ($\overline{\mathrm{Nu}}$) to the experiments is also found.

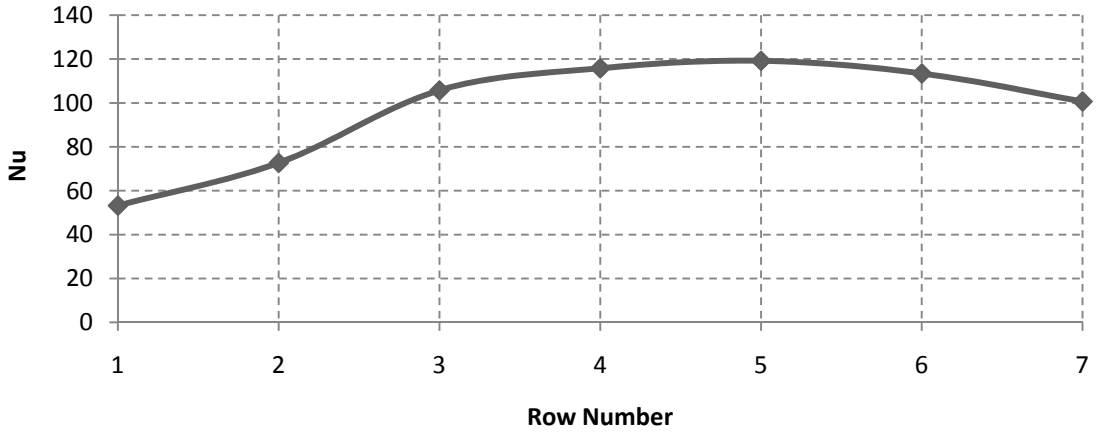

Figure 5-5: Nu development through the channel

5.4 Particle Transport in Developing Flow

5.4.1 Particle Simulation Parameters

The input parameters for the particle model are shown in Table 5-1, which include the important geometrical parameters, the hydrodynamic conditions and properties of the sand particles. The hydrodynamic conditions are set to simulate a cooling channel within a gas turbine blade. Three non-dimensional particle diameters of 0.002, 0.004, and 0.01 are investigated. The respective Stokes numbers (St_p) are 0.78, 3.1 and 19.5. In addition to these three particle sizes, three non-dimensional softening temperatures (θ_{ST}) of 0, 0.37 and 0.67 for particles with $St_p = 0.78$ are simulated to investigate the effect of θ_{ST} on deposition. The thermal stokes numbers show that convection will dominate the heat transfer by several orders of magnitude for all particle sizes. In all cases, there are 110,000 particles injected upstream of the pin fins. The particles are uniformly distributed in the flow cross-section and the simulation is run until all particles have passed through the end of the pin fin channel. The end of the pin fin array was set to x = 9 which is approximately 2D downstream from the center of the last pin.

Table 5-1: Input parameters for particle model

L^*_{ref} (D)	1
u^*_{ref} (u^*_{max})	1
Inlet Temperature	$\theta = 0$
Wall Temperature	$\theta_w = 1$
Pressure	20 atm
Density (Air)	7.06 kg/m^3
c_p (Air)	1141 J/kgK
k_f (Air)	66.7 x 10^{-3} W/mK
Non-dimensional Diameter (Sand)	0.002, 0.004, 0.01
Density (Sand)	1650 kg/m^3
c_p (Sand)	800 J/kgK
θ_{ST} (Sand)	0, 0.37, 0.67
St_p	0.78, 3.1, 19.5 (eqn. 2-12)
St_{conv}	0.57, 2.3, 14.4 (eqn. 2-16)
St_{rad}	244 , 487, 1221 (eqn. 2-17)

5.4.2 Effect of particle size on erosion at $\theta_{ST} = 0.67$

The sand particle's Stokes number which varies with particle size has a major effect on both the deposition and erosive behavior of particles. Looking first at erosion, the total number of particle impacts on surfaces is tabulated in Table 5-2. These include both erosive particles (particles which on impact have a temperature lower than the softening temperature) and deposited particles. It is noted that for the Stokes numbers of 3.1 and 19.5, a very small percentage of particles are deposited, hence Table 5-2 mostly represents erosive impacts for these two particle sizes. It is also noted that the total number of impacts are larger than the number of particles injected and the difference between the two increases as the particle size increase. This is because a single particle can have multiple impacts with the surfaces of the channel and pins as it bounces around. The table shows that as the particle size is increased, the percentage of

impacts with pins is increased from 50.2% for St_p = 0.78 to 79.1% for St_p = 19.5. This increase in pin impacts with particle size is due to the increased inertia and energy in the larger particles and their inability to change with the flow around them; therefore, the larger particles are more likely to have multiple collisions with the pins mostly leading to erosive wear.

Table 5-2: Total collision results for St_p = 0.78, 3.1 and 19.5 (θ_{ST} = 0.67)

	0.78	3.1	19.5
Total Number of particle impacts	203293	414837	404645
Number of pin impacts	101918	271504	319999
Percentage of pin impacts	50.2%	65.5%	79.1%
Number of impacts on channel walls	101375	143333	84646
Percentage of impacts on channel walls	49.8%	34.5%	20.9%

Figure 5-6 shows the percentage of the total particle impacts per pin row. In this and subsequent figures, the 8th pin row is the wall area after the last pin row extending 2D from the center of the last pin, since there are only 7 rows in the geometry. The St_p = 0.78 particles show the largest variation in the number of impacts with pin rows. They show few impacts with the first row and then a large increase in impacts at the second row. This increase can be attributed to the acceleration of the flow around the first pin and into the 2nd row. The particles entrained in the accelerated flow are unable to avoid the 2nd row as they do for the 1st row. This results in more impacts with the 2nd row. After the 2nd row, the impacts reduce and then increase to a near constant value after the fifth row. This evening out in the number of impacts is a further indication that the flow is developed by the fifth pin. For the larger particles there are few collisions at the first row but after the 1st row there is a large increase and an essentially constant percentage of impacts afterwards. This is due to the fact that after impact the larger particles are controlled less by the flow and more by their momentum. The lack of impacts in row 8 is due to the simple fact that there are no pins to collide with.

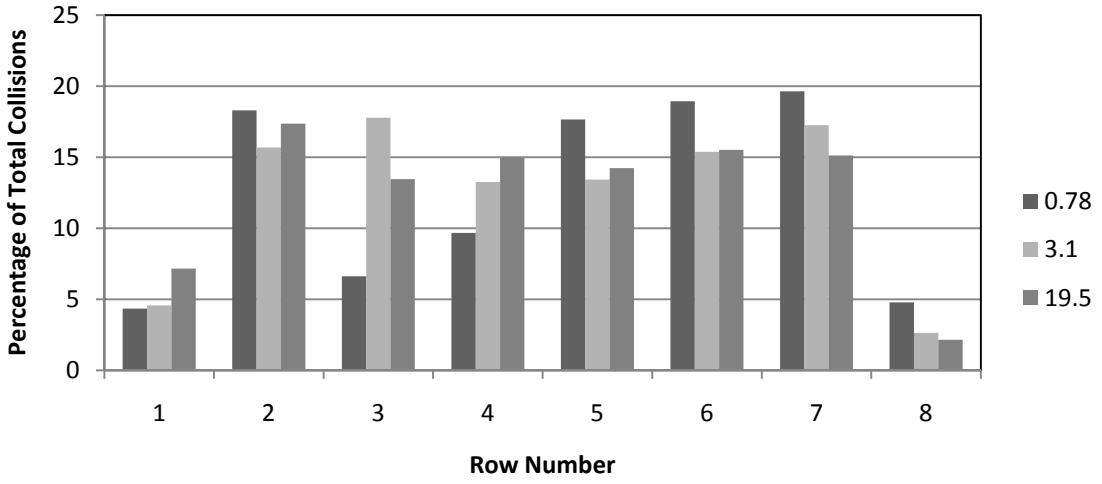

Figure 5-6: Percentage of total particle impacts per row (θ_{ST} = 0.67)

Figure 5-7 shows a side trace of all impacts for each Stokes number, where every dot represents an impact of a particle. For the St_p = 0.78 particles, most particle impacts are along the front face of the pin with much fewer impacts on the back of the pins. The rear impacts also appear closer to the channel walls than toward the center of the pin. After the fourth pin there is also larger coverage of the pin, which coincides with the fully turbulent nature of the flow in this region which leads to more particle dispersion.

The St_p = 3.1 particles continue this trend of most impaction at the frontal face of the pins. Overall, this Stokes number shows more coverage of the front face from the first row onward. The rear face of the pins in rows two and three show an increased number of impacts as compared to the St_p = 0.78 particles. Also, the St_p = 3.1 particles show increased impacts near walls on the rear face of the pins just as with the 0.78 Stokes number. However, after row 3, there are a reduced number of rear impacts on the pins. This reduction in rear impacts is accompanied by the flow approaching a fully developed state with smaller wake recirculation zones.

The St_p = 19.5 particles show the largest impaction coverage on the pins. All rows for these particles have both front and rear particle impacts. Rows 3 through 6 are almost completely covered in particle

impacts. This complete coverage is due to the fact that when St_p = 19.5 particles strike a pin and bounce off, the large momentum of the particle carries it upstream where it collides with the back of the pin in the preceding row. The fluid flow has little influence on the particle and the particle continues on its trajectory until another collision with a pin. This observation can also be seen from the fully developed particle results. In that case, there are no particle deposits on the rear of the pins when assuming perfect capture. Thus, the bouncing of the particles is what causes the collisions. Also, this mechanism of impaction for the St_p = 19.5 particles is evident from the absence of impaction at the rear of the last pin row.

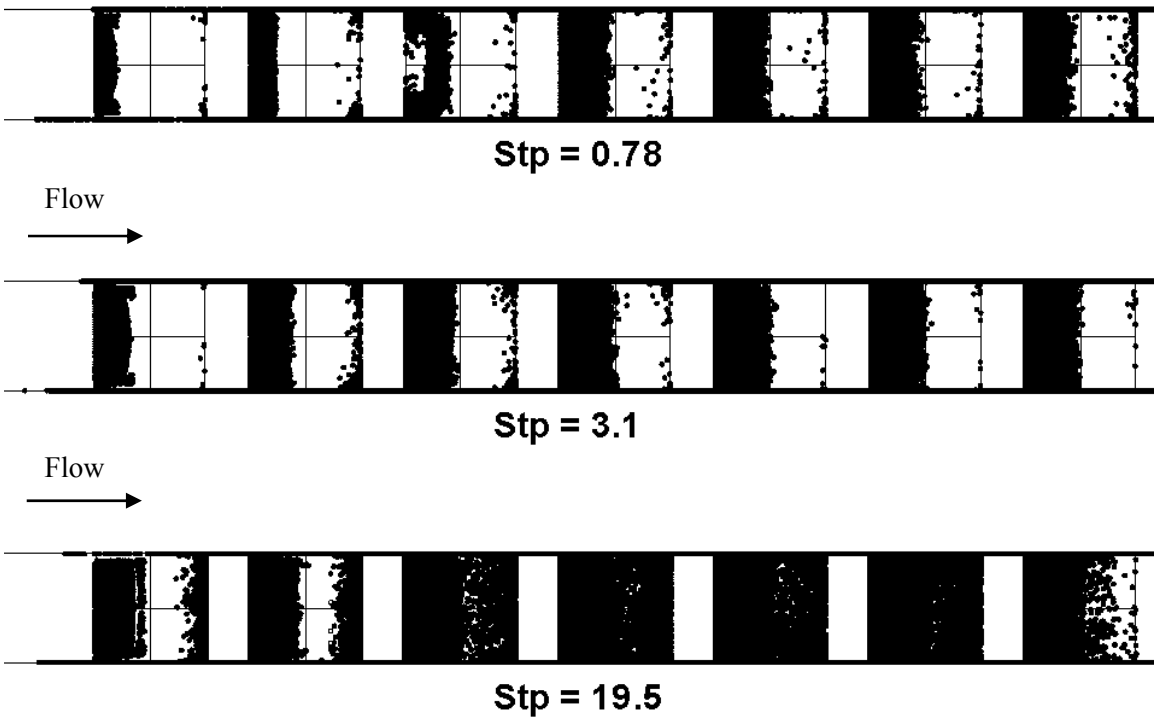

Figure 5-7: Side view of impact traces for the St_p = 0.78, 3.1 and 19.5 (θ_{ST} = 0.67)

Figure 5-8 gives a plot of the channel wall particle impacts for St_p = 0.78, 3.1 and 19.5 with the particles colored based on their impact angle, alpha (90° is normal to surface). For the St_p = 0.78 particles, most of the particle impacts occur with a very shallow angle of impact of about 5-10°. In the region of

the horseshoe vortex, the angle is increased due the particles becoming entrained in the vortex and impacting at a higher angle. As the flow develops more, the region of increased impact angle grows. The plot also shows that wake regions of the developing flow are less populated with particles than the fully developed regions of the pin fin array.

The $St_p = 3.1$ particles show a reduced influence of the horseshoe vortex on the particles. Throughout the domain the region of influence of the horseshoe vortex is reduced to an area directly in front of the pin and does not continue significantly along the sides of the pin as in the $St_p = 0.78$ case. Again in the wake region for the 2nd row, only the primary recirculation region is populated with particles and is populated more so than for the $St_p = 0.78$ particles. This increased population was seen also on the side impact traces (Figure 5-7). The wake regions in the more developed regions of the array (Rows 4-7) show less population as compared to the $St_p = 0.78$ particles which was also shown by the side traces (Figure 5-7). The reason for this is that with the increased Stokes number, the particles are less influenced by the weaker developed wake region behind the pin and do not enter the recirculation zone as the particles did for the stronger wakes in the developing flow region.

The $St_p = 19.5$ particles show little dependence on the flow features. The downstream rows show no influence of the horseshoe vortex as compared to the smaller particles. However, there is an increase in the average impact angle in the more developed regions of the flow. The wake regions are completely populated with particle impacts suggesting that particles bouncing off downstream pins impact the channel walls also. The wake region of the last pin row shows fewer impacts on the channel walls as it did behind the pin in Figure 5-7.

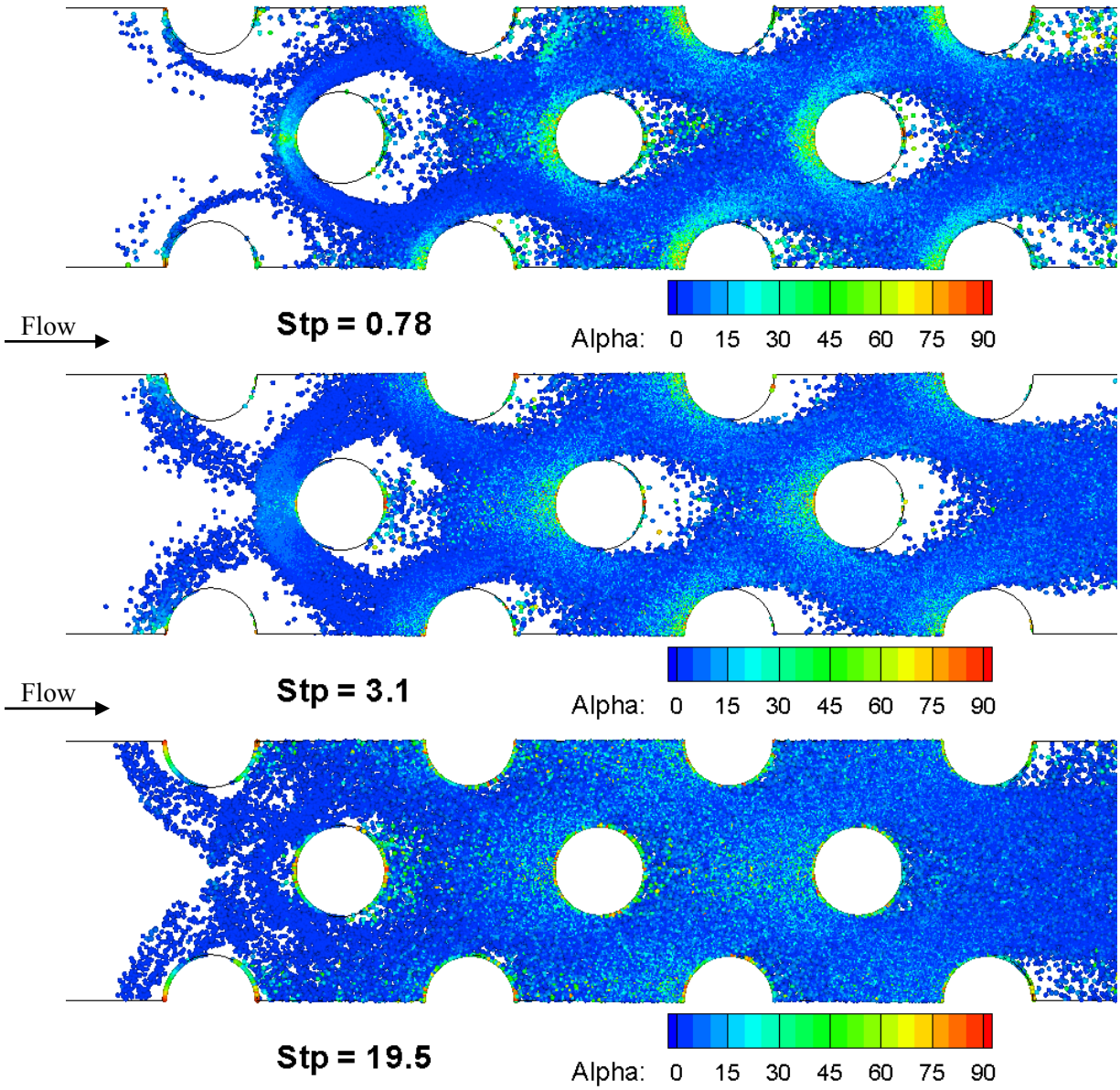

Figure 5-8: Particle impact traces on the channel walls for St_p = 0.78, 3.1 and 19.5 particles with particle coloring based on impact angle, alpha

To estimate the amount of erosive energy that could potentially be transferred to the surfaces, the energy fraction of erosive particles (EFEP) is defined. EFEP is an idealized measure which uses the normal impact velocity of the particle, the particle mass and the number of particles impacting to measure the total kinetic energy of impact. This is then normalized by the total kinetic energy of the incoming

particles. The impacts with surfaces are all assumed elastic (restitution coefficient = 1) and particles may impact pins multiple times. The energy imparted by the particle to the surface is assumed to be total kinetic energy available (restitution coefficient = 0). With these assumptions, the EFEP for this simulation may be above 1, i.e. there is more particle energy imparted to surfaces than incoming to the domain. This would suggest that the particles extract energy from the fluid flow; however this is not accounted for in the calculations under the assumption that in reality the erosion happens over a long operational period and that the particle concentration is dilute. EFEP represents a worst case scenario and is a useful measure to compare the erosive potential of different particle sizes. It is noted that the incoming energy of a particle with a Stokes number of 19.5 is 125 times that of a particle with a Stokes number of 0.78 by virtue of its increased diameter and therefore mass.

The EFEP results for the three Stokes numbers are given in Table 5-3. The results show that for all three cases the EFEP of the pin is at least 1-2 orders of magnitude higher than the channel walls, which is to be expected as the pin is impacted head on at high impact angles, whereas the channel walls are impacted at shallower angles, in addition to the larger number of impacts on the pin. This suggests that the pins are much more likely to erode than the channel walls. The highest EFEP is for $St_p = 3.1$ with $St_p = 19.5$ being 10% less. Again this does not mean that the $St_p = 19.5$ particles impart less energy but that of the available incoming energy a higher fraction is transferred to the surfaces by the 3.1 Stokes number particles.

Table 5-3: EFEP results for $St_p = 0.78$, 3.1 and 19.5 ($\theta_{ST} = 0.67$)

	0.78	3.1	19.5
Total EFEP	0.584	2.305	2.054
Pin EFEP	0.575	2.265	2.045
Channel Wall EFEP	0.009	0.040	0.009

Figure 5-9 gives the pin EFEP per row for the 0.78, 3.1 and 19.5 Stokes numbers. The St_p = 0.78 particles show a much smaller EFEP magnitude than the larger particle sizes. The EFEP follows the same trend as the number of impacts for all particles. Essentially this means that the impacts on the pins are approximately similar in both impact velocity and angle for all rows and the EFEP for this geometry can be directly correlated to the number of impacts.

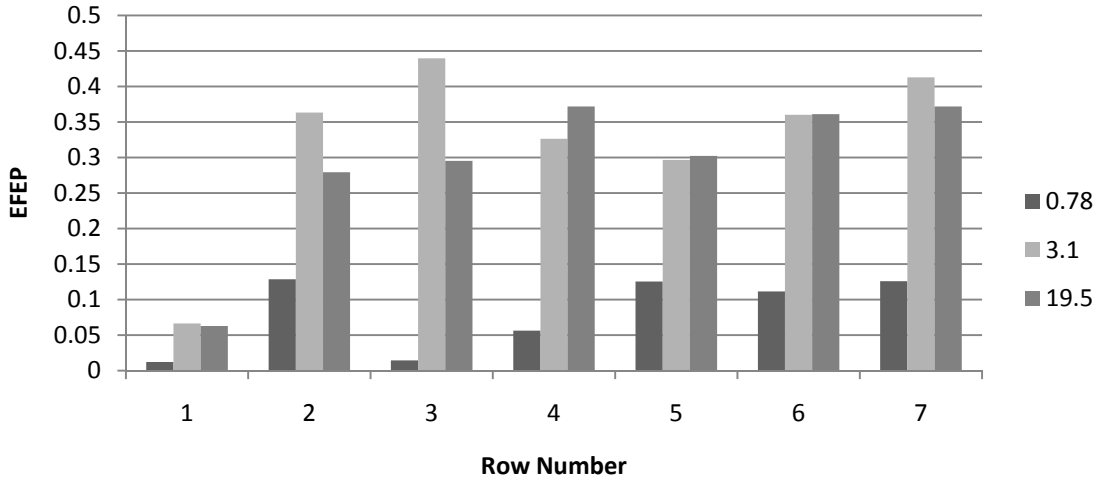

Figure 5-9: Pin EFEP per row for the St_p = 0.78, 3.1 and 19.5 particles (θ_{ST} = 0.67)

5.4.3 Effect of particle size on deposition at θ_{ST} = 0.67

With the erosive behavior of the particle quantified for the varying Stokes numbers, the deposition can be explored. Table 5-4 shows the results of varying Stokes number on the deposition of particles. Particles deposit on the surfaces if their temperature is above the softening temperature θ_{ST}. At the entrance, the particles are at the inlet temperature ($\theta = 0$) of the fluid and gradually pick up heat from the walls ($\theta = 1$) of the channel as the carrier phase heats up in the channel. The smaller the thermal Stokes number of the particles the faster they will react to changes in the surrounding fluid temperature. For all three Stokes numbers, the number of pin deposits is extremely small compared to the total number of particles injected (110,000). The St_p = 0.78 particles show the highest number of both pin and channel

depositions at 14,770. The $St_p = 19.5$ particles show the fewest with 5 which are all on the channel wall. Deposition can only occur if the particles are entrained in a region near the channel wall with sufficient residence time for their temperature to increase beyond the softening temperature. The preference for channel wall deposition suggests two things. First, the particles are more likely to be entrained close to the wall region and thus have their temperature increase significantly. Secondly, the particles do not spend sufficient time near pin surfaces to heat up and deposit.

Figure 5-10 shows the percentage of total deposited particles per pin row for the $St_p = 0.78$, 3.1 and 19.5 particles. Except for the $St_p = 19.5$ particles, which have only 5 total deposits, all on the 2nd row channel wall, the other particle sizes show a similar trend. There are few deposits in the 1st and 2nd rows then a large jump in deposits at the 3rd row. This is followed by a slight reduction in deposits before a nearly linear rise over the last four rows. This rise in the end rows is attributed to the increased fluid temperature and thus particle temperature as the particles travel through the channel. Therefore, there is an increased likelihood of deposition.

Table 5-4: Total deposition results for $St_p = 0.78$, 3.1 and 19.5. ($\theta_{ST} = 0.67$)

	0.78	3.1	19.5
Total number of deposits	14770	3880	5
Percentage of total particles (out of 110,000)	13.4%	2.8%	0.005%
Number of pin deposits	57	12	0
Percentage of pin deposits from total deposits	0.4%	0.3%	0%
Number of deposits on channel walls	14713	3868	5
Percentage of deposits on channel walls from total deposits	99.6%	99.7%	100%

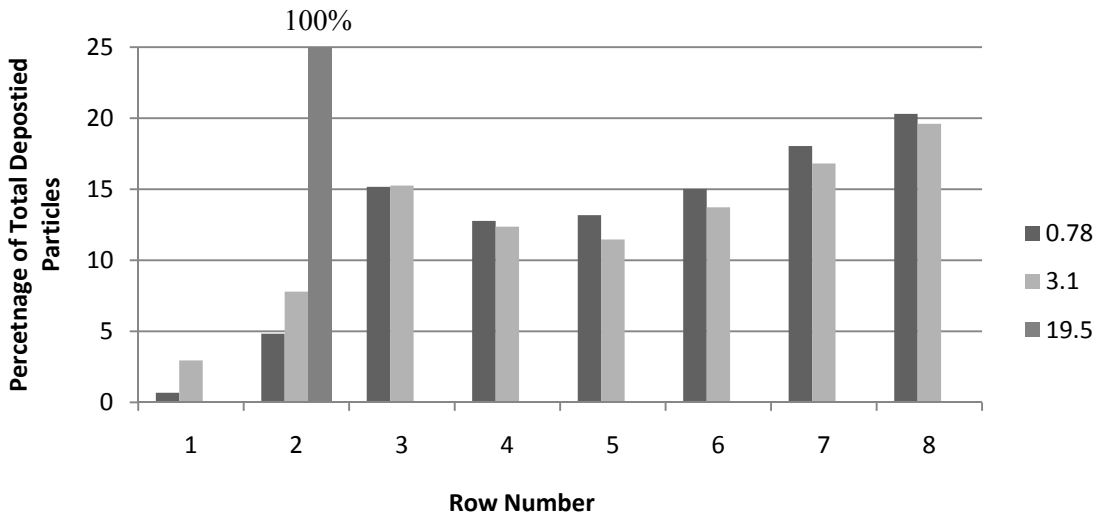

Figure 5-10: Percentage of total deposited particles per row for St_p = 0.78, 3.1 and 19.5 (θ_{ST} = 0.67)

5.4.4 Effect of Softening Temperature on Erosion for St_p = 0.78 particles

The first investigation is into how varying the θ_{ST} will affect the erosive characteristics of the particles. Three different softening temperatures using a particle Stokes number of 0.78 were investigated. These were θ_{ST} equal to 0, 0.33 and 0.67. Table 5-5 shows results for the number of impacts for the different θ_{ST} values. For the θ_{ST} of 0, there will be no erosion since every particle impact results in a deposition and the results are the same as the deposition results. For the θ_{ST} = 0.37 case there was a 9.5% reduction in the total number of impacts as compared to the θ_{ST} = 0.67 case. Most of this reduction is due to fewer channel wall impacts as the number of collisions with pins is similar between the two different θ_{ST}. This reduced number of channel wall hits is complemented by the increased number of depositions seen for a θ_{ST} of 0.37. Figure 5-11 shows the percentage of particle impacts per row for each θ_{ST}. The general trend for all three temperatures is the same with a few differences. All softening temperatures show an increase in impacts on the 2nd row and then an increase again when the flow becomes developed. The θ_{ST} = 0 softening temperature has a higher percentage of impacts on the 2nd pin and fewer on every other pin as compared to the other θ_{ST}. This reduction in impacts in the downstream rows is due to the reduced

number of particles available for impact since every impact is a deposit. The 0.37 and 0.67 softening temperatures are much closer in the percentage of impacts per row over the whole array.

Table 5-5: Total impact results for the θ_{ST} = 0, 0.37 and 0.67 (St_p = 0.78)

	0	0.37	0.67
Total number of impacts	87228	183996	203293
Number of pin impacts	61033	105738	101918
Percentage of pin impacts	70.0%	57.5%	50.2%
Number of impacts with channel walls	26195	78258	101375
Percentage of impacts with channel walls	30.0%	42.5%	49.8%

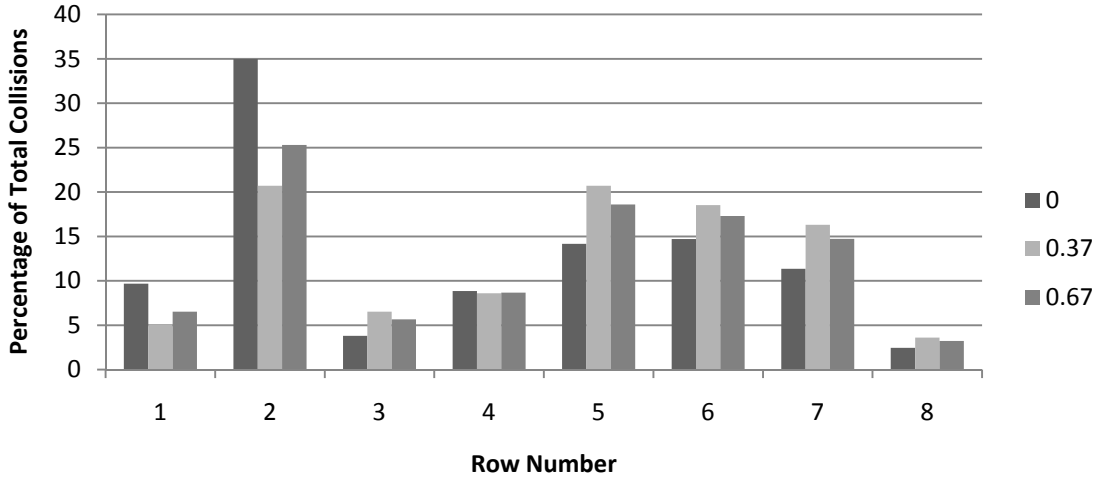

Figure 5-11: Percentage of particle impacts per row for varying softening temperatures (St_p = 0.78)

5.4.5 Effect of Softening Temperature on Deposition for St_p = 0.78 particles

Table 5-6 shows the results of this differing softening temperature on particle depositions. As expected, raising the softening temperature reduces the number of total deposits, while increasing deposition on the channel walls as a fraction of the total deposits. Figure 5-12 shows the percentage of deposited particles per row for each θ_{ST}. For the θ_{ST} = 0 temperature, most particles are deposited when they hit the 2nd row. There is also a rise in depositions when the flow becomes developed around the 4th pin. The θ_{ST} = 0.37 and θ_{ST} = 0.67 temperatures show a similar trend where both softening temperatures show a gradual

increase across the channel due to the increase in particle temperature as it travels through the channel. The $\theta_{ST} = 0.37$ deposition does increase faster in the leading rows due to the less restrictive deposition criteria and maintains a higher percentage per row than the $\theta_{ST} = 0.67$ except in the area behind the last pin.

Table 5-6: Total deposition results for $\theta_{ST} = 0$, 0.37 and 0.67 ($St_p = 0.78$)

	0	0.37	0.67
Total number of deposits	87228	40881	14770
Percentage of total particles	73.9%	37.2%	13.4%
Number of pin deposits	61033	1746	57
Percentage of deposits on pins from total deposits	70.0%	4.3%	0.4%
Number of deposits on channel walls	26195	39135	14713
Percentage of deposits on channel from total deposits	30.0%	95.7%	99.6%

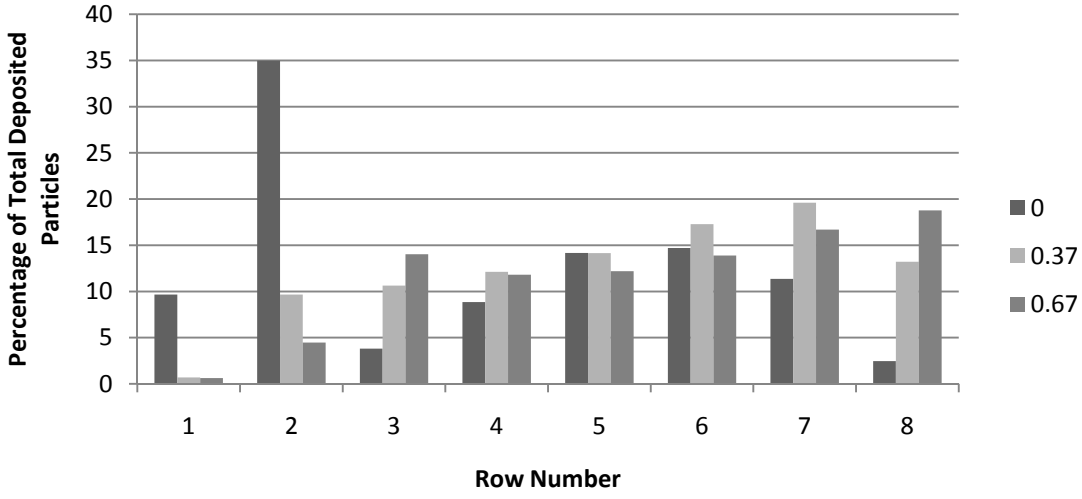

Figure 5-12: Percentage of deposited particles per row for varying softening temperatures ($St_p = 0.78$)

Chapter 6
Summary and Conclusion

The deposition and erosive characteristics of sand particles within a pin fin array were investigated in both a developing and fully developed fluid field. Along with the particles, the fluid and heat transfer characteristics of the pin fin array were also investigated. The generalized multiblock code, GenIDLEST, was used for all simulations using LES to capture the effects of turbulence. The particle tracking was completed using a Lagrangian framework where the particle trajectory was calculated using the current fluid field.

The first step in the investigation was to validate the fluid solver with known experimental results. For this, a fully developed pin fin array was used with streamwise and spanwise spacings of 1.5D and 2.5D respectively. The height of the channel was equal to the pin diameter, D. Reynolds numbers based on the pin diameter and u_{max} velocity ranged from approximately 2500 to 9700. Overall, the simulations over predict both the experimental friction factor and Nusselt number. The friction factor was within the error bounds of the correlation used. For the Nusselt number, the differences could be explained by inexact experimental boundary conditions and differences in measurement and calculation techniques. However, the simulation matched all trends from experiments well.

The next case investigated was a fully developed pin fin array with streamwise and spanwise spacings of 1.414D and 2.828D respectively. The fluid results agreed with the expected trends. The heat transfer increased due to the reduced pin spacing while the friction factor stayed relatively constant as is predicted by the experiments. A total of 10,000 particles were then injected into the fully developed array with a Reynolds number of 9700. The number of particle traverses was tracked to see how far the particles traveled in the streamwise direction. The deposition model was set such that every wall collision was a deposit. Two Stokes numbers of 0.38 and 9.62 were investigated. The lower Stokes number particles

showed reduced deposition (85% of total particles) owing to the fact that the particles could more readily adjust to the flow around them. The higher Stokes number particles could not readily avoid the pins and thus were readily deposited (97% of total particles). The percentage of deposits on the pins was also dependent on Stokes number with 54% and 78% for the lower and higher Stokes numbers, respectively.

The final case investigated was that of a developing pin fin array. Here the same basic core geometry of the fully developed case was used and repeated to create 7 pin rows. The flow was allowed to develop within the rows as is the case in a gas turbine. The Reynolds number was set to 15,740. The fluid field showed a fully developed state around the 4^{th} pin row. The heat transfer characteristics showed a similar trend which matches well to the experimental data. The Nusselt number distribution on the pin surface also compared well with the experimental findings. Overall, the average Nusselt number was found to be 97.3 for the array which is within 4.3% of Metzger's correlation for average Nusselt number at this streamwise spacing.

110,000 particles were then injected into the developing flow pin fin array. Three Stokes numbers of 0.78, 3.5 and 19.5 were investigated as well as three different non-dimensional softening temperatures of 0, 0.37 and 0.67. Deposition was shown to increase with decreasing Stokes number from 0.05% for the largest Stokes number to 13.4% for the smallest. Almost all deposition occurred on the channel walls. The reason for this is that the particles have a much higher residence time near the hot walls and can attain a temperature high enough to deposit. The particles behavior within the array was also drastically different with different Stokes numbers. The higher Stokes number particles were shown to bounce off pins and project upstream even as far as the previous pin rows. The lower Stokes number particles while still impacting the pin were quickly turned by the flow and continued downstream. Varying the softening temperature also had a major effect on the deposition behavior. As expected, lowering the softening temperature increased deposition ranging from 79% to 13.4% from the lowest to highest softening temperatures. With a decreasing softening temperature the number of particle depositing on pins also

increased since the particle needed less residence time to reach a temperature greater than the softening temperature.

The characteristics of the deposition and erosion would be that the particles are most likely to deposit on the channel wall and most likely to erode the pin surfaces. Both of these phenomena could have major consequences on the heat transfer characteristics of the pin fin array and thus the durability of the turbine blades. The hope is that this work can aid in the understanding of particle behavior and help guide future designs to mitigate particle deposition and erosion.

Bibliography

1. Hamed, A., W. Tabakoff, and R. Wenglarz, *Erosion and deposition in turbomachinery.* Journal of Propulsion and Power, 2006. **22**(2): p. 350-360.
2. Metzger, D.E.B., R.A.; Bronson J.P. , *Developing heat transfer in rectangular ducts with staggered arrays of short pin fins.* J HEAT TRANSFER TRANS ASME, 1982. **104**(4): p. 700-706.
3. Metzger, D.E., Z.X. Fan, and W.B. Shepard. *Pressure Loss and Heat Transfer through Multiple Rows of Short Pin Fins*. 1982. Munich, Ger: Hemisphere Publ Corp.
4. Metzger, D.E. and S.W. Haley. *Heat transfer experiments and flow visualization for arrays of short pin fins*. 1982. London, Engl: ASME.
5. Armstrong, J. and D. Winstanley, *Review of staggered array pin fin heat transfer for turbine cooling applications.* Journal of Turbomachinery, 1988. **110**(1): p. 94-103.
6. Chyu, M.K., *Heat transfer and pressure drop for short pin-fin arrays with pin-endwall fillet.* Transactions of the ASME. Journal of Heat Transfer, 1990. **112**(4): p. 926-32.
7. Chyu, M.K., et al., *Heat transfer contributions of pins and endwall in pin-fin arrays: Effects of thermal boundary condition modeling.* Journal of Turbomachinery, 1999. **121**(2): p. 257-263.
8. Ames, F.E., L.A. Dvorak, and M.J. Morrow, *Turbulent augmentation of internal convection over pins in staggered-pin fin arrays.* Transactions of the ASME. The Journal of Turbomachinery, 2005. **127**(1): p. 183-90.
9. Healy, J.V., *Perturbed two-phase cylindrical type flows.* Physics of Fluids, 1970. **13**(3): p. 551-7.
10. Vittal, B.V.R. and W. Tabakoff, *Two-phase flow around a two-dimensional cylinder.* AIAA Journal, 1987. **25**(5): p. 648-54.
11. Tian, Z.F., J.Y. Tu, and G.H. Yeoh, *Numerical modelling and validation of gas-particle flow in an in-line tube bank.* Computers & Chemical Engineering, 2007. **31**(9): p. 1064-1072.
12. Morsi, Y.S., et al., *Principal characteristics of turbulent gas-particulate flow in the vicinity of single tube and tube bundle structure.* Chemical Engineering Science, 2004. **59**(15): p. 3141-3157.
13. Jun, Y.-D. and W. Tabakoff. *Numerical simulation of a dilute particulate flow over tube banks*. 1992. Anaheim, CA, USA: Publ by ASME.
14. Fan, J., et al., *Numerical computation of particle-laden gas flows past staggered tube banks undergoing erosion.* Powder Technology, 1994. **80**(1): p. 1-10.
15. Jin, J., et al., *Numerical simulation of the tube erosion resulted from particle impacts.* Wear, 2001. **250-251**(PART 1): p. 114-119.
16. Shah, A. and D.K. Tafti, *Transport of particulates in an internal cooling ribbed duct.* Transactions of the ASME. The Journal of Turbomachinery, 2007. **129**(4): p. 816-25.
17. Shah, A. and D.K. Tafti. *Transport of particulates in a rotating internal cooling ribbed duct*. 2006. Miami, FL, United states: American Society of Mechanical Engineers.
18. Tafti, D.K. *GenIDLEST - A scalable parallel computational tool for simulating complex turbulent flows*. 2001. New York, NY 10016-5990, United States: American Society of Mechanical Engineers.
19. Tafti, D.K., *Time-accurate techniques for turbulent heat transfer analysis in complex geometries, Advances in Computational Fluid Dynamics and Heat Transfer*, R. Amano and B. Sunden, Editors. 2009, WIT Press: Southampton Uk.
20. Germano, M., et al., *A dynamic subgrid-scale eddy viscosity model.* Physics of Fluids A (Fluid Dynamics), 1991. **3**(7): p. 1760-5.

21. Najjar, F.M. and D.K. Tafti, *Study of discrete test filters and finite difference approximations for the dynamic subgrid-scale stress model.* Physics of Fluids, 1996. **8**(4): p. 1076-88.
22. Portela, L.M. and R.V.A. Oliemans, *Eulerian-Lagrangian DNS/LES of particle-turbulence interactions in wall-bounded flows.* International Journal for Numerical Methods in Fluids, 2003. **43**(9): p. 1045-65.
23. Klienstreuer, C., *Two Phase Flow: Theory and Application*. 1st ed. 2003: Taylor and Francis Books, Inc.
24. Armenio, V. and V. Fiorotto, *The importance of the forces acting on particles in turbulent flows.* Physics of Fluids, 2001. **13**(8): p. 2437-40.
25. Schiller, L. and A. Nauman, Z. Ver. Dtsch. Ing, 1933. **77**: p. 318-320.
26. McLaughlin, J.B., *Aerosol particle deposition in numerically stimulated channel flow.* Physics of Fluids A (Fluid Dynamics), 1989. **1**(7): p. 1211-24.
27. Incropera, F.P., Dewitt, D.P., Bergman, T.L., Lavine, A.S., *Fundamentals of Heat and Mass Transfer*. 6th ed. 2007: John Wiley and Sons.
28. Zhu, B., et al. *Internal cooling inside an L-shaped duct with pin-fin turbulators under rotating and non-rotating conditions with and without sand particles*. 2007. Montreal, Que., Canada: American Society of Mechanical Engineers.